



Cite this: *Nanoscale*, 2022, **14**, 15217

## Recent advances in high-crystalline conjugated organic polymeric materials for photocatalytic CO<sub>2</sub> conversion

Fengyi Yang,<sup>a</sup> Jiafu Qu,<sup>a</sup> Yang Zheng,<sup>c</sup> Yahui Cai,<sup>id</sup><sup>b</sup> Xiaogang Yang,<sup>id</sup><sup>a</sup> Chang Ming Li<sup>id</sup><sup>a</sup> and Jundie Hu<sup>id,\*a</sup>

The photocatalytic conversion of carbon dioxide (CO<sub>2</sub>) to high-value-added fuels is a meaningful strategy to achieve carbon neutrality and alleviate the energy crisis. However, the low efficiency, poor selectivity, and insufficient product variety greatly limit its practical applications. In this regard, conjugated organic polymeric materials including carbon nitride (g-C<sub>3</sub>N<sub>4</sub>), covalent organic frameworks (COFs), and covalent triazine frameworks (CTFs) exhibit enormous potential owing to their structural diversity and functional tunability. Nevertheless, their catalytic activities are largely suppressed by the traditional amorphous or weakly crystalline structures. Therefore, constructing relevant high-crystalline materials to ameliorate their inherent drawbacks is an efficient strategy to enhance the photocatalytic performance of conjugated organic polymeric materials. In this review, the advantages of high-crystalline organic polymeric materials including reducing the concentration of defects, enhancing the built-in electric field, reducing the inter-layer hydrogen bonding, and crystal plane regulation are highlighted. Furthermore, the strategies for their synthesis such as molten-salt, solid salt template, and microwave-assisted methods are comprehensively summarized, while the modification strategies including defect engineering, element doping, surface loading, and heterojunction construction are elaborated for enhancing their photocatalytic activities. Ultimately, the challenges and opportunities of high-crystalline conjugated organic polymeric materials in photocatalytic CO<sub>2</sub> conversion are prospected to give some inspiration and guidance for researchers.

Received 29th August 2022,  
Accepted 23rd September 2022

DOI: 10.1039/d2nr04727f  
[rsc.li/nanoscale](http://rsc.li/nanoscale)

### 1. Introduction

The excessive emission of CO<sub>2</sub> has caused irreversible harm to the environment, such as the greenhouse effect, climate change, rising sea levels, and marine ecological destruction.<sup>1</sup> According to the World Meteorological Organization, the CO<sub>2</sub> concentration has exceeded 400 ppm, and many global extreme climate records are being broken. Simultaneously, energy shortage is another crisis accompanying the rapid consumption of fossil fuels. In this regard, low-carbon sustainable development strategies, including energy saving and emission reduction, renewable energy, and carbon capture and storage, have been launched worldwide.<sup>2,3</sup> Therefore, how to effectively reduce the CO<sub>2</sub> content while developing a sustainable carbon-neutral economy is a valuable approach. In this case, directly converting CO<sub>2</sub> into high-value-added hydrocarbon fuels or

chemicals (e.g., CO, CH<sub>4</sub>, CH<sub>3</sub>OH, HCOOH, HCHO, C<sub>2</sub>H<sub>5</sub>OH, and C<sub>2</sub>H<sub>4</sub>) has proven to be an effective way, where many technologies can be employed including organic catalysis,<sup>4</sup> electrocatalysis,<sup>5,6</sup> photocatalysis,<sup>7,8</sup> biocatalysis,<sup>9</sup> thermocatalysis,<sup>10</sup> and photoenzymatic catalysis.<sup>11</sup> Among these, artificial photosynthesis to achieve photocatalytic CO<sub>2</sub> reduction is an extremely promising route due to its advantages of clean, eco-friendly, green and mild conditions, *etc.*<sup>12-14</sup> As we all know, the energy provided by the sun in one hour far exceeds the energy consumption of all human beings in one year. Therefore, efficient photocatalytic CO<sub>2</sub> conversion can simultaneously alleviate the two global challenges of environment and energy.<sup>15</sup>

Photocatalysts are the critical factor to achieve efficient CO<sub>2</sub> conversion, which involves a series of complex processes including light-harvesting, separation and transfer of photo-generated charge carriers, adsorption and activation of CO<sub>2</sub>, and redox reactions on the surface of catalysts. However, it is difficult to improve the reactivity and selectivity of photocatalytic CO<sub>2</sub> conversion due to the thermodynamic stability of the CO<sub>2</sub> molecule (dissociation energy of C=O bond: ~750 kJ mol<sup>-1</sup>) and complex intermediates and products (Fig. 1). Therefore, an ideal photocatalyst is one that can satisfy both

<sup>a</sup>School of Materials Science and Engineering, Suzhou University of Science and Technology, Suzhou 215009, China. E-mail: [hjd@usts.edu.cn](mailto:hjd@usts.edu.cn)

<sup>b</sup>College of Materials Science and Engineering, Nanjing Forestry University, Nanjing 210037, China

<sup>c</sup>State Key Laboratory of Organometallic Chemistry, Shanghai Institute of Organic Chemistry, Chinese Academy of Sciences, Shanghai 200032, China

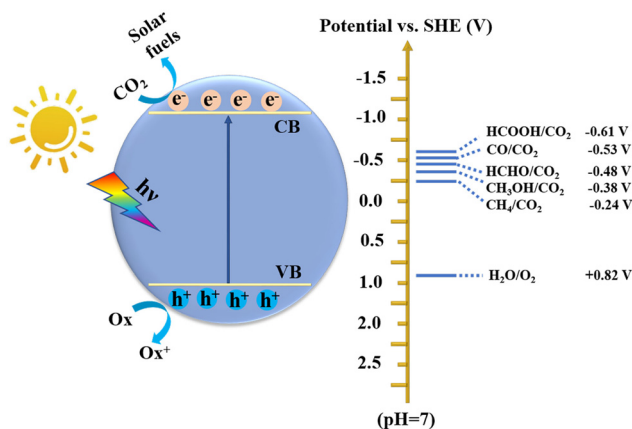


**Fig. 1** Schematic diagram of photocatalytic  $\text{CO}_2$  reduction over a semiconductor.

the thermodynamic and kinetic conditions of  $\text{CO}_2$  conversion. At present, many inorganic semiconductor materials including metal oxides,<sup>16–18</sup> sulfides,<sup>19,20</sup> nitrides,<sup>21,22</sup> and perovskite halides<sup>23</sup> have been shown to be effective catalysts for  $\text{CO}_2$  conversion. Nevertheless, compared with organic polymeric materials, inorganic materials are difficult for adjusting band structures (including band gap, conduction band, and valence band), narrow visible light absorption range, and rapid recombination of photogenerated carriers, which greatly limit their catalytic efficiency and product selectivity.<sup>24</sup> Although their band structure can be changed by element doping,<sup>25</sup> this process is very cumbersome. In contrast, organic semiconductor materials exhibit numerous advantages.<sup>26</sup>

Conjugated organic polymeric materials such as graphite carbon nitride ( $\text{g-C}_3\text{N}_4$ ),<sup>27,28</sup> covalent organic frameworks

(COFs),<sup>29</sup> covalent triazine frameworks (CTFs),<sup>30</sup> and conjugated microporous polymers (CMPs)<sup>31</sup> are arousing interests from researchers because of their tunable molecular or electronic structure,<sup>32</sup> adjustable band gap by controlling different monomers,<sup>33,34</sup> excellent visible light response, and unique properties of photocarrier separation and transport enabled by their  $\pi$  conjugated stacking structures. For example,  $\text{g-C}_3\text{N}_4$  is a graphene-like semiconductor, which shows good photochemical stability due to the strong covalent bond between carbon and nitrogen.<sup>35</sup> COFs have a periodic arrangement, uniform apertures and precise adjustable structures, and their physical and chemical properties can be accurately regulated by combining specific groups or molecules.<sup>36</sup> CTFs are a new type of porous metal-free material with an ordered structure, large specific surface area, diverse structure and stable physical and chemical properties.<sup>37</sup> These conjugated organic polymeric materials all show great potential for photocatalytic  $\text{CO}_2$  conversion, and thus are widely reported in the literature. However, most of the reported organic polymer photocatalysts are amorphous or possess low crystallinity, which greatly affects the separation and transport of charge carriers, limiting their photocatalytic activities.<sup>38</sup> Crystallinity is an important factor affecting the photoreactivity of conjugated organic polymeric materials because high crystallinity can effectively improve their photoelectric kinetics by eliminating defects, enhancing the built-in electric field, reducing the interlayer hydrogen bonding and regulating the crystal planes.<sup>39–42</sup> Thus, the construction of high-crystalline conjugated organic polymeric materials is a promising strategy to achieve enhanced photocatalytic  $\text{CO}_2$  conversion.

Herein, we review the recent advances in high-crystalline conjugated organic polymeric materials for photocatalytic  $\text{CO}_2$  conversion. Firstly, we comprehensively review the synthesis



*Fengyi Yang is currently a Postgraduate at Suzhou University of Science and Technology. Her current research direction is on photoenzymatic catalytic carbon dioxide conversion reactions.*

**Fengyi Yang**



**Chang Ming Li**

*Chang Ming Li is a Professor and the Director of School of Materials Science and Engineering in Suzhou University of Science and Technology, China. His main research interests involve cross-field sciences including functional nanomaterials and green energies. He has published more than 700 peer-reviewed journal papers with more than 30 000 citations and H-index of 85 as well as 240 patents. He is a Fellow of the American Institute of Medicine and Biological Engineering, Foreign Member of the Russian Academy of Engineering and Fellow of the Royal Society of Chemistry, serving as an Editorial Board Member of RSC Advances, member of Advisory Board for Nanoscales, RSC and Joule, Cell as well as the Chief Editor of Materials on Energy.*

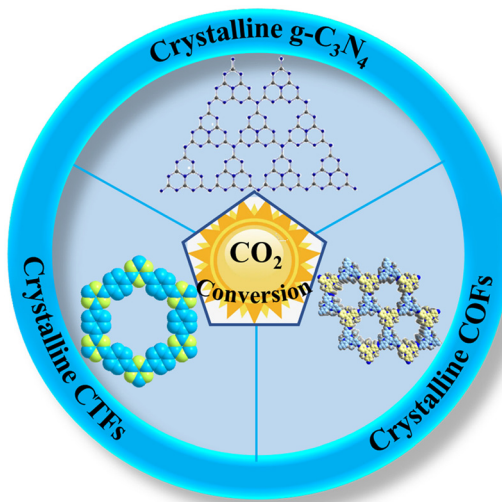


Fig. 2 Overview of high-crystalline conjugated organic polymeric materials for the photocatalytic conversion of  $\text{CO}_2$ .

methods of high-crystalline conjugated organic polymeric materials (mainly focusing on crystalline  $\text{g-C}_3\text{N}_4$ , COFs and CTFs) for convenient reference (Fig. 2). Then, the advantages of high-crystalline conjugated organic polymeric materials are elaborated, which will provide theoretical guidance for the design of efficient photocatalysts. Some modification strategies and applications of high-crystalline conjugated organic polymeric materials for improved  $\text{CO}_2$  conversion are summarized, especially the relationship between crystallinity and  $\text{CO}_2$  conversion performance is emphasized. Finally, the current problems and challenges in this field are summarized, and the future development prospects of high-crystalline conjugated organic polymeric materials in photocatalytic  $\text{CO}_2$  conversion are discussed.



Jundie Hu

Jundie Hu received her PhD at the College of Chemistry, Chemical Engineering and Materials Science from Soochow University in 2019 under the supervision of Prof. Jianmei Lu. Subsequently, she joined Suzhou University of Science and Technology as an Associate Professor. Her current research interests mainly focus on engineering nanoporous materials including 2D materials, heterojunctions, conjugated organic

polymeric materials, and their applications in photocatalysis, such as water splitting, carbon dioxide conversion, and environmental remediation.

## 2. Synthesis of high-crystalline conjugated organic polymeric materials

At present, high-crystalline conjugated organic polymeric materials are arousing interest from researchers, and thus many methods have been developed to synthesize these high-crystalline materials. More importantly, different synthetic methods will affect the structure, size and morphology of the catalysts, which in turn affect the photocatalytic performance of the photocatalysts. In the case of the common  $\text{g-C}_3\text{N}_4$  materials, they are mainly prepared *via* high-temperature pyrolysis, solvothermal method and physicochemical vapor deposition, and their precursors are usually small nitrogen-containing molecules. Other organic polymers including COFs, CTFs, and CMPs are synthesized by coupling two or more different monomers, generally by coupling reactions and condensation reactions.<sup>43,44</sup> Now, most COFs are synthesized in solvothermal systems under harsh conditions. However, most of them possess low crystallinity or are amorphous. In this section, the main synthetic methods for high-crystalline conjugated organic polymeric materials are summarized according to the classification of different materials (such as  $\text{g-C}_3\text{N}_4$ , COFs and CTFs).

### 2.1 Synthesis of crystalline $\text{g-C}_3\text{N}_4$

In the early stages, the  $\text{g-C}_3\text{N}_4$  first applied for photocatalytic water splitting and hydrogen ( $\text{H}_2$ ) evolution was amorphous,<sup>45</sup> and its  $\text{H}_2$  yield was very low even with the use of Pt as a cocatalyst. The main reason for this is that  $\text{g-C}_3\text{N}_4$  with low crystallinity exhibits poor light absorption, slow electron transport, and rapid recombination of photogenerated carriers. Thus, to solve this problem, various common methods to synthesize highly crystalline  $\text{g-C}_3\text{N}_4$  have been developed, such as molten salt method, microwave-assisted method and solid salt template method.

Different precursors have an effect on the formation of the crystalline phase. For example, many highly crystalline  $\text{g-C}_3\text{N}_4$  possessing triazinyl groups have been synthesized from dicyandiamide,<sup>46</sup> and heptazine highly crystalline  $\text{g-C}_3\text{N}_4$  can usually be prepared using melamine as the precursor system.<sup>47</sup>

The different methods for the synthesis of highly crystalline  $\text{g-C}_3\text{N}_4$  have advantages and disadvantages. For example, the molten salt method, which is one of the most widely used methods to synthesize high-crystalline  $\text{g-C}_3\text{N}_4$ , is easy to perform, simple, environmentally friendly, *etc.*; however, this method requires a large amount of molten salt, water-sensitive salt  $\text{LiCl}$ , and its yield is relatively low. Different from the widely used molten salt method employing multiple salts, with the use of a single salt as a template, its limited space can guide the growth of  $\text{g-C}_3\text{N}_4$  and yield  $\text{g-C}_3\text{N}_4$  samples with high crystallinity and obvious long-range periodicity and large grain size. Also, the modification temperature is lower than the melting point of the salt, and thus this method is milder.<sup>48</sup>

**2.1.1 Molten-salt method.** Since the 1960s, molten salts have been found to be an effective reaction medium for the

synthesis of certain organic compounds. Inspired by this, Bojdys *et al.* adopted the ion thermal method to prepare crystalline g-C<sub>3</sub>N<sub>4</sub> for the first time.<sup>49</sup> The original C<sub>3</sub>N<sub>4</sub> is usually obtained by the polymerization of monomers at high temperature (500–600 °C), which is a typical solid-state reaction process.<sup>50</sup> However, the mass transfer of reactants is slow, and the resulting products usually have low crystallinity. The molten salt method differs from the traditional wet chemical method in that it involves the use of ionized and/or anions as the solvent, and the molten salt provides a wide operating temperature range of 200 °C to 1000 °C, allowing the controlled synthesis of covalent compounds.<sup>51</sup> The melting point of eutectic salt is much lower than the condensation point of *s*-heptazine, which can completely melt the precursor. Generally, the melting point of the salt in the molten salt method is lower than the condensation point for the formation of the polymer, while the melting point of the salt in the salt template method is higher than the condensation temperature. Thus, the molten salt method has been widely used for the synthesis of highly crystalline g-C<sub>3</sub>N<sub>4</sub> because of its advantages of simple operation, mild condition, environmental protection and powerful function.<sup>51</sup> Among the salts employed, binary alkali metal chlorides (*e.g.*, LiCl/KCl, NaCl/LiCl, and NaCl/KCl) are often used as the molten salts due to their high temperature stability, non-corrosion and relatively low melting point. The general preparation process is divided into two forms, as follows: (1) two-step method and (2) one-step method.

On the one hand, in the two-step method, nitrogen-rich precursors (*e.g.*, dicyandiamide, melamine, and urea) are ther-

mally polymerized to form large blocks of g-C<sub>3</sub>N<sub>4</sub>, and the bulk g-C<sub>3</sub>N<sub>4</sub> is mixed with molten salts for secondary pyrolysis to obtain crystalline g-C<sub>3</sub>N<sub>4</sub>.<sup>52</sup> The current crystalline g-C<sub>3</sub>N<sub>4</sub> mainly includes two structures of poly(triazine imides) (PTI) and poly(heptazine imides) (PHI). Bhunia *et al.* prepared highly crystalline PTI for improved photocatalytic hydrogen generation using melamine and 2,4,6-triaminopyrimidine as precursors to obtain g-C<sub>3</sub>N<sub>4</sub>, and then LiCl and KCl as molten salts to get PTI.<sup>53</sup> Studies also showed that the stability of triazine-based g-C<sub>3</sub>N<sub>4</sub> is less than heptazine-based g-C<sub>3</sub>N<sub>4</sub><sup>54,55</sup> because heptazine has a larger  $\pi$  conjugated system, which is beneficial to widen the light absorption range, promote the charge migration rate, and enhance the photocatalytic activity. With the assistance of hydrochloric acid, Li *et al.* obtained bulk g-C<sub>3</sub>N<sub>4</sub> by thermal polymerization with melamine, and then synthesized heptazine structure g-C<sub>3</sub>N<sub>4</sub> (HCCN) with KCl and LiCl as molten salts and found that the amount of hydrochloric acid can change the crystallinity and surface defects of g-C<sub>3</sub>N<sub>4</sub> by removing the K<sup>+</sup> ions from the terminal amino. Furthermore, the high crystallinity of g-C<sub>3</sub>N<sub>4</sub> was confirmed in its TEM images (Fig. 3a),<sup>52</sup> where the clear lattice fringes indicate the successful regulation of high crystallization in g-C<sub>3</sub>N<sub>4</sub>.

On the other hand, the one-step molten-salt method involves mixing the precursors for the preparation of g-C<sub>3</sub>N<sub>4</sub> with molten salts for calcination. For example, in our recent work, crystalline g-C<sub>3</sub>N<sub>4</sub> was synthesized *via* a one-step molten salt method. In detail, electron-deficient 5-aminotetrazolium was used as the precursor and NaCl/KCl as the molten salt, and a well-ordered CNA nanoarray was obtained by high-temperature polymerization. These results show that the highly crys-

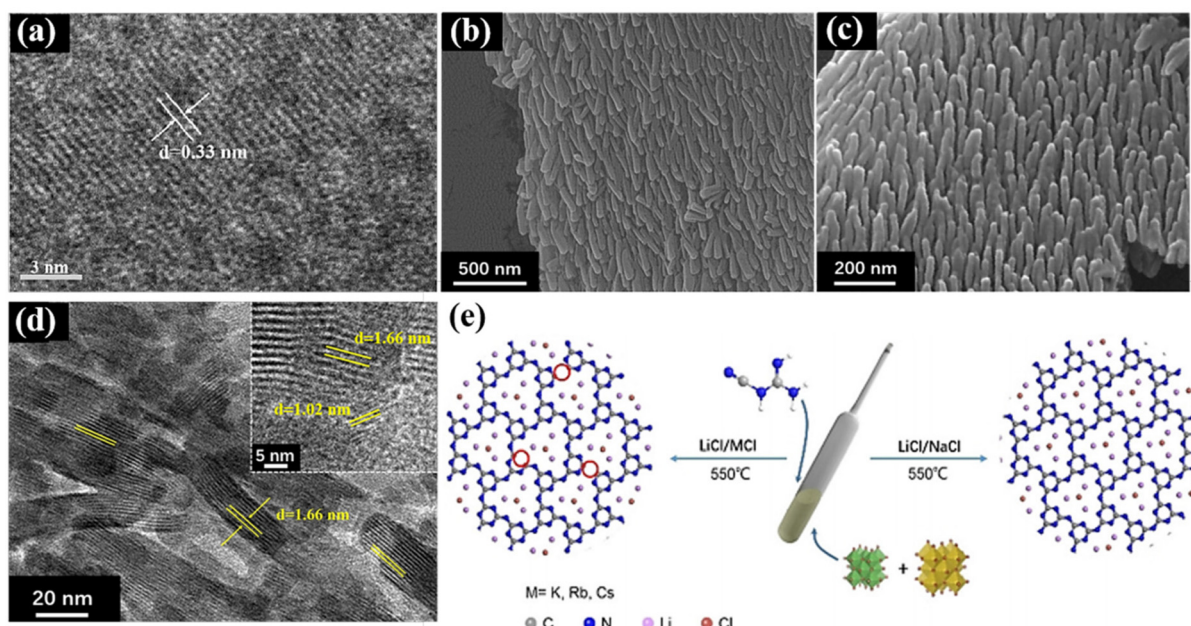
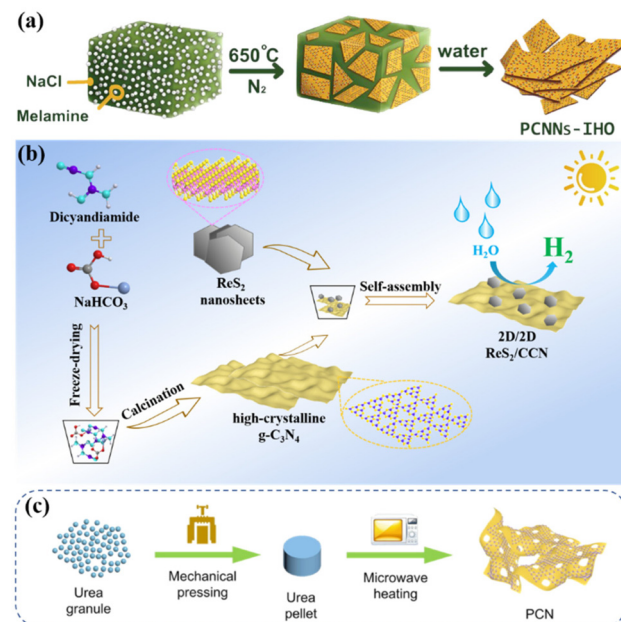


Fig. 3 (a) HRTEM images of CCN. Reproduced from ref. 52 with permission from the Chinese Academy of Sciences, Copyright 2020. (b and c) SEM images of CAN. Reproduced from ref. 57 with permission from Elsevier, Copyright 2022. (d) HRTEM images of CNA (inset is the enlarged part). Reproduced from ref. 57 with permission from Elsevier, Copyright 2022. (e) Proposed salt melt synthetic processes of PTI/Li<sup>+</sup>Cl<sup>-</sup> catalyst using different binary alkali metal chlorides with different melting points. Reproduced from ref. 51 with permission from Wiley-VCH, Copyright 2021.

talline  $\text{g-C}_3\text{N}_4$  synthesized by the molten salt method also has a certain effect on the morphology of  $\text{g-C}_3\text{N}_4$ , where  $\text{g-C}_3\text{N}_4$  is transformed from the general bulk or nanosheets to nanorods (Fig. 3b–d). It is speculated that the reason for the formation of this rod-like shape is the accumulation in the molten salt state. The adhesion between  $\text{NaCl}/\text{KCl}$  and heptazine is relatively low, and thus the nanorod structure was formed in the space of the salt. In addition, as shown in Fig. 3e, Liu *et al.* used an  $\text{LiCl}/\text{NaCl}$  binary salt as the molten salt to synthesize crystalline  $\text{g-C}_3\text{N}_4$ , provided milder reaction conditions because its melting point is very close to the polymerization temperature.<sup>51</sup> Dotssova *et al.* synthesized potassium-doped PHI using triazole derivatives as the precursors *via* the melt salt method, which showed improved visible light absorption and changed electronic structure.<sup>56</sup>

**2.1.2 Solid salt template method.** The solid salt template method is another effective strategy to synthesize highly crystalline  $\text{g-C}_3\text{N}_4$ , which can easily regulate its morphology, structure, and specific surface area. The synthesis process of a single salt is simpler than that of multi-heavy salts, and the construction and optimization of highly crystalline  $\text{g-C}_3\text{N}_4$  can be realized simultaneously (here, this refers to the element doping). New crystalline  $\text{g-C}_3\text{N}_4$  can be synthesized *via* the solid salt constrained growth and pyrolysis control. Because the melting point of the solid salt is higher than the reaction temperature, a solid salt can be used as a template. For example, Qiu *et al.* used solid  $\text{KBr}$  as a solid template for the growth of crystalline  $\text{g-C}_3\text{N}_4$ . Because the melting point of solid  $\text{KBr}$  ( $730\text{ }^\circ\text{C}$ ) is higher than the reaction temperature ( $580\text{ }^\circ\text{C}$ ), a high molar ratio of salt and precursor provides a confined space, which led to the growth of crystalline  $\text{g-C}_3\text{N}_4$  in the salt crystal to form a crystal structure. In addition, the salt can also act as a reactant to insert cations into the product.<sup>58</sup> Various experimental studies have also proven the versatility of this method, that is, different single salts can be used as templates, such as  $\text{KCl}$  and  $\text{NaCl}$ . For example, Yuan *et al.* used  $\text{KCl}$  as the salt template to prepare highly crystalline  $\text{g-C}_3\text{N}_4$  with a heptazine structure in one simple step, where the amount of  $\text{KCl}$  could change the electronic structure and band gap of  $\text{g-C}_3\text{N}_4$ .<sup>59</sup> Unlike the commonly used  $\text{LiCl}/\text{KCl}$  molten salt,  $\text{KCl}$  with a high melting point can be used as the salt template, making it easier to control the construction of a K gradient. Zhang *et al.*<sup>60</sup> successfully inserted a  $\text{K}^+$  ion gradient into the heptazine-based molecular chains using three basic K salts. Compared with general  $\text{g-C}_3\text{N}_4$ , the K-doped crystalline  $\text{g-C}_3\text{N}_4$  (K-CN) had a lower electrostatic potential in all directions, indicating that K-CN has a better electron transport performance, which also benefits from its crystal structure, where the melon chain has a more orderly arrangement of heptazine and shorter layer spacing, and the  $\text{K}^+$  ions can act as a “bridge” to boost charge transfer. The lattice fringes of K-CN can also be observed by high-resolution transmission electron microscopy (HRTEM). Moreover, Huo *et al.* used  $\text{NaCl}$  as an ion induction and template agent and mesoporous melon as a raw material for the preparation of the PHI structure and highly  $\text{Na}^+$ -doped crystal  $\text{g-C}_3\text{N}_4$ , which significantly enhanced



**Fig. 4** (a) Illustration of the synthesis process of PCNNs-IHO by on-surface polymerization. Reproduced from ref. 62 with permission from Wiley-VCH, Copyright 2021. (b) Schematic illustration of constructing crystalline  $\text{g-C}_3\text{N}_4$  by salt template method. Reproduced from ref. 63 with permission from Elsevier, Copyright 2022. (c) Schematic illustration of microwave thermolysis of urea pellets. Reproduced from ref. 42 with permission from Elsevier, Copyright 2021.

the separation of light raw charge.<sup>61</sup> As shown in Fig. 4a, Guo *et al.* prepared polymer carbon nitride nanosheets with an in-plane highly ordered structure (PCNNs-IHO) *via* the polymerization of melamine on the  $\text{NaCl}$  crystal surface at high temperature using  $\text{NaCl}$  as the salt template.<sup>62</sup> In addition, in our work, highly crystalline  $\text{g-C}_3\text{N}_4$  was synthesized *via* the template-mediated method, which used  $\text{NaHCO}_3$  as the template mediator and dicyandiamide as the precursor (Fig. 4b). The improvement in its catalytic performance was mainly due to the removal of deep defects by highly crystalline  $\text{g-C}_3\text{N}_4$ .<sup>63</sup>

**2.1.3 Other methods.** In addition to the above-mentioned methods, there are many methods for the synthesis of high-crystalline  $\text{g-C}_3\text{N}_4$ . The microwave-assisted method is a simple and rapid method to synthesize high-crystalline  $\text{g-C}_3\text{N}_4$ . The microwave-assisted pyrolysis method can generate  $\text{g-C}_3\text{N}_4$  within only a few minutes due to the strong rotation, friction and collision of N-rich molecules under microwave irradiation, which greatly improves the crystallinity (Fig. 4c).<sup>42,64,65</sup> The preparation of crystalline  $\text{g-C}_3\text{N}_4$  *via* this method is also beneficial to control its visible light response range and photocatalytic activity.<sup>42,66</sup>

Some materials with tunable nanostructures are often prepared by using some templates such as the inexpensive and versatile porous anodic alumina (AAO). Li *et al.* used AAO templates impregnated with a mixture of cyanamide and distilled water to limit the synthesis of  $\text{g-C}_3\text{N}_4$  nanorods (CNRs) through thermal condensation within a single nanochannel, thereby improving the crystallinity of  $\text{g-C}_3\text{N}_4$ .<sup>67</sup>

## 2.2. Synthesis of crystalline COFs

Since the first report on COFs by Cote *et al.* in 2005,<sup>68</sup> COFs have been widely used in photocatalysis due to their high porosity, large specific surface area, wide visible light absorption range and strong charge separation ability. Compared with some amorphous conjugated organic polymeric materials, the highly ordered  $\pi$ -electron channels in COFs enable better carrier transport. Therefore, crystalline COFs have attracted significant attention because of their unique structures and properties. However, the construction of crystalline COFs is a great challenge due to their poor reversibility. At present, crystalline COFs are mainly synthesized *via* the solvothermal method, microwave-assisted method, sonochemical method, vapor-assisted conversion, ionothermal, interfacial polymerization, *etc.*

**2.2.1 Solvothermal method.** The solvothermal method is the most common method to prepare COFs, which can be realized by some condensation reactions. It is a relatively mild and controllable method. In the solvothermal synthesis process, water or an organic solvent is used as the reaction medium, and it is usually carried out in a closed system at a temperature above the boiling point of the solvent.<sup>69</sup> The high-crystalline COFs can be obtained *via* solvothermal synthesis. In 2011, Uribe-Romo *et al.* developed hydrazine linked COFs based on the condensation of a Schiff base using 2,5-diethoxy hydrazine terephthalate and 1,3,5-triformylbenzene, or a mixture of 2,5-diethoxy hydrazine terephthalate and 1,3,5-tri(4-

formylphenyl) benzene as raw materials to prepare COF-42 and COF-43 *via* the reversible condensation by dehydration in a flame-sealed tube, respectively. This hydrazine-bonded organic unit formed a two-dimensional trigonal layer (Fig. 5a) with high crystallinity, excellent chemical, and thermal stability, which showed great potential for a wide range of applications.<sup>70</sup> As shown in Fig. 5b, Huang *et al.* dispersed 2,4,6-tris (4-formylphenyl)-1,3,5-triazine in a mixture of dimethyl xylene, 1,4-dioxane and acetic acid aqueous solution and heated it for 72 h under autogenous pressure, and COFs with higher crystallinity were obtained and their photocatalytic activity was further enhanced by filling PdIn nanoclusters (named Pd<sub>x</sub>In<sub>y</sub>@N<sub>3</sub>-COF).<sup>71</sup> However, the most significant disadvantage of this method is that it takes a long time, usually three days. Afterwards, several studies reported that interlamellar hydrogen bonding is beneficial to enhance the crystallinity and stability of COFs.<sup>72</sup> For instance, Chen *et al.* proved that interlamellar hydrogen bonding is beneficial to improve the crystallinity, physical properties and photochemical activity of porphyrin COFs.<sup>73</sup> Li *et al.* synthesized three different crystalline COFs using 1,3,5-triformylbenzene (Tf) as the linker and three building units with similar structures but different rigidity as precursors. This method can be used to synthesize high-crystalline hydrazide COFs under robust and harsh conditions, which was confirmed by the clear lattice stripes in the HRTEM images (Fig. 5c–e).<sup>74</sup> Recently, Zhang *et al.* reported a general and scalable protocol to prepare robust, highly crystalline

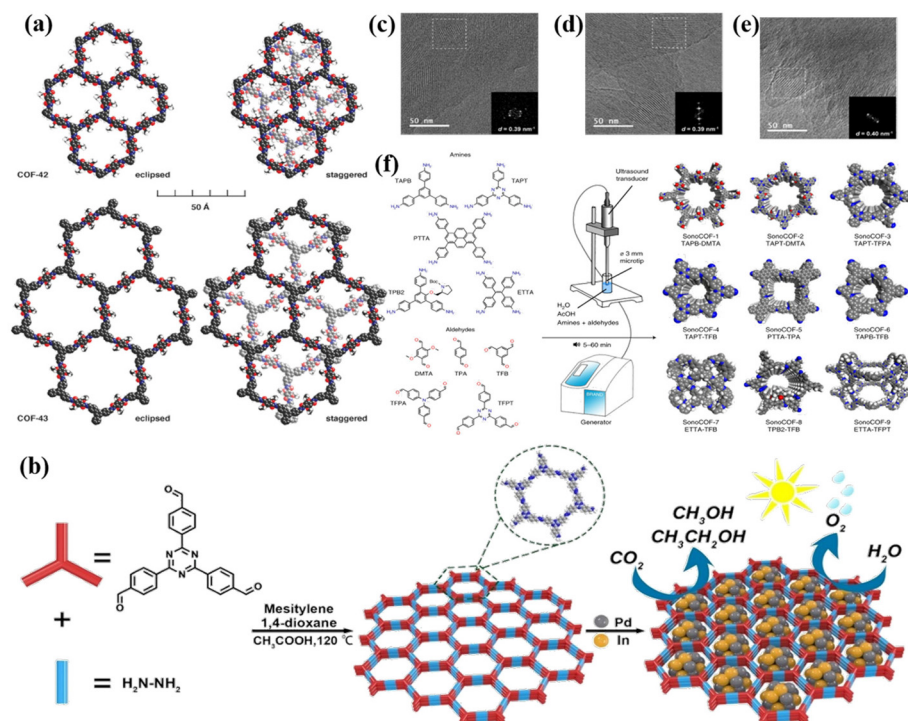


**Fig. 5** (a) Space-filling models of COF-42 and COF-43. Reproduced from ref. 70 with permission from the American Chemical Society, Copyright 2011. (b) Synthesis of PdIn@N<sub>3</sub>-COF. Reproduced from ref. 71 with permission from Elsevier, Copyright 2021. (c–e) TEM images of high-crystalline hydrazide COFs. Reproduced from ref. 74 with permission from the American Chemical Society, Copyright 2020. (f) Apparatus and conditions used for sonochemical synthesis, the COFs studied and the monomers used to synthesize them. Reproduced from ref. 83 with permission from Springer, Copyright 2022.

imine COFs under a simple vacuum-free synthetic procedure, in which the monomers were pre-organization *via* a reversible and removable covalent tether. The reconstructed COFs exhibited greatly improved crystallinity and higher porosity, resulting in improved charge carrier transport and photocatalytic performance.<sup>29</sup> Thus, the design of highly crystalline COFs can be realized by the atomic structure-controlled programming of organic materials.

**2.2.2 Microwave-assisted method.** Compared with the traditional external heating method, the biggest feature of microwave synthesis technology is the short reaction time and easy handling process.<sup>75</sup> Campbell *et al.* manufactured crystalline COF-5 *via* the microwave-assisted method, where 1,4-benzenediboronic acid and 2,3,6,7,10,11-hexahydroxytri-phenylene were employed as the precursors and a mixture of mesitylene and 1,4-dioxane as the solvent. The microwave synthesis method speeds up the reaction time by about 200-times than the solvothermal method, resulting in purer products and higher yields. Also, the temperature and pressure could be controlled in the microwave reactor. In addition, the surface area of crystalline COF-5 obtained by the microwave synthesis method was significantly higher than that of the material prepared by the solvothermal method.<sup>76</sup> Wei *et al.* further confirmed that the microwave method can effectively improve the yield of COFs by preparing TpPa-COF(MW), where the synthesis time was significantly shortened, and the product exhibited good porosity and high crystallinity. Thus, the microwave-assisted method is an efficient and fast method to provide high-quality crystalline COF materials.<sup>77</sup>

**2.2.3 Interfacial polymerization.** Interfacial synthesis<sup>78</sup> is a commonly used method to synthesize polymer films, but it is still a challenge to fabricate highly crystalline organic polymer films. Therefore, Kaushik *et al.* developed an interface crystallization method at room temperature to synthesize crystalline COF films. Using liquid-liquid interface as a template, salt-mediated technology [amine-*p*-toluene sulfonic acid (PTSA) salt] was introduced to control the interface reaction rate to control the crystallinity, and the defect-free high-crystalline COF film was finally obtained.<sup>79</sup>

**2.2.4 Vapor-assisted conversion.** For the application of COFs in all aspects, it is ideal to control the thickness, morphology and crystallinity of the grown COF films. The new steam-assisted conversion method at room temperature provides a convenient method for the synthesis of high-crystallinity COF membrane materials. In this method, the reaction precursor is deposited on the substrate as a dry gel, and then exposed to steam to initiate the reaction. Medina *et al.* formed a series of highly ordered 2D COF films based on the co-condensation of boric acid and hexahydroxytriphenylene (HHTP) under mild conditions. The films were crystalline and exhibited random crystalline orientations on different surfaces.<sup>80</sup>

**2.2.5 Mechanical ball milling.** Mechanochemical bonding is a simple, economical and environmentally friendly way to construct COFs. Biswal *et al.* synthesized highly stable COFs *via* mechanical ball milling under solvent-free conditions at room temperature.<sup>81</sup> Li *et al.* synthesized an imide COFs *via* an efficient and convenient ball milling method based on the

polymerization of 1,3,5-trichlorobenzene and diamine. Compared with the traditional solvothermal method, the mechanical ball milling method requires less time and little or no organic solvent.<sup>82</sup> However, the COFs synthesized by this method have a lower specific surface area, and thus lower application potential.

**2.2.6 Other methods.** Furthermore, the sonochemical method is a low-energy consumption and time-saving method to prepare COF materials. Sonochemical reactions are driven by high-energy ultrasonic waves. The method of acoustic chemistry is a feasible method for the rapid synthesis of COFs due to its high synthesis speed, simplicity, versatility and high quality of synthesized materials. As shown in Fig. 5f, Zhao *et al.* reported a strategy for the rapid synthesis of imine-linked COFs using acoustic chemistry in acetic acid aqueous solution. The reaction time was very short, and in addition, the crystallinity and porosity of the obtained COFs were better than that obtained by the conventional solvothermal method.<sup>83</sup> Compared with the solvothermal synthesis of COFs, this method avoids the use of organic solvents and is safer and simpler.

### 2.3 Synthesis of crystalline CTFs

Covalent triazine frameworks are promising catalysts due to their unique triazine structure, abundant porosity, high conjugation, and excellent chemical and thermal stability, exhibiting great potential in the field of photocatalysis. In 2008, Thomas *et al.* synthesized a series of polymers with triazine bonds by condensation reaction, and first proposed the concept of CTFs.<sup>84</sup> However, similar to the above-mentioned g-C<sub>3</sub>N<sub>4</sub> and COFs, the CTFs synthesized at present are mostly low-crystalline or amorphous, while the methods for synthesizing high-crystalline CTFs are limited, which are discussed in this section.

**2.3.1 Molten-salt method.** The molten salt method is the classic method for the synthesis of CTFs. In most instances, an aromatic nitrile monomer and molten zinc chloride are used as raw materials to obtain crystalline CTFs by ion thermal polymerization. In this process, the melted ZnCl<sub>2</sub> at 400 °C is a good catalyst for the trimer reaction. For example, Bojdys and colleagues synthesized CTF-2 by heating zinc chloride and 2,6-naphthalene ethyl bicarbonate at 400 °C for 40 h. An ordered, tightly packed structure was obtained at lower temperatures.<sup>85</sup> However, there are two drawbacks to the above-mentioned method for the preparation of CTFs, *i.e.*, when the temperature is above 300 °C, the products would be agglutinated and undesirable carbonization occurs. In this regard, Lan *et al.* synthesized CTF-ES<sub>T</sub> *via* the ion-thermal method using a mixture of ternary eutectic salt NaCl-KCl-ZnCl<sub>2</sub> with a melting point of about 200 °C as the molten salt (Fig. 6a). These milder conditions not only promoted the polycondensation process but also avoided carbonization. Compared with CTF-1 (obtained from the cyclotrimerization of 1,4-dicyanobenzene) synthesized in pure ZnCl<sub>2</sub>, the ordered crystalline CTF-ES<sub>T</sub> exhibited a better photocatalytic hydrogen evolution performance. Subsequently, different CTFs samples were obtained by increasing the polycondensation temperature from 200 °C to 400 °C, and the color of the samples turned

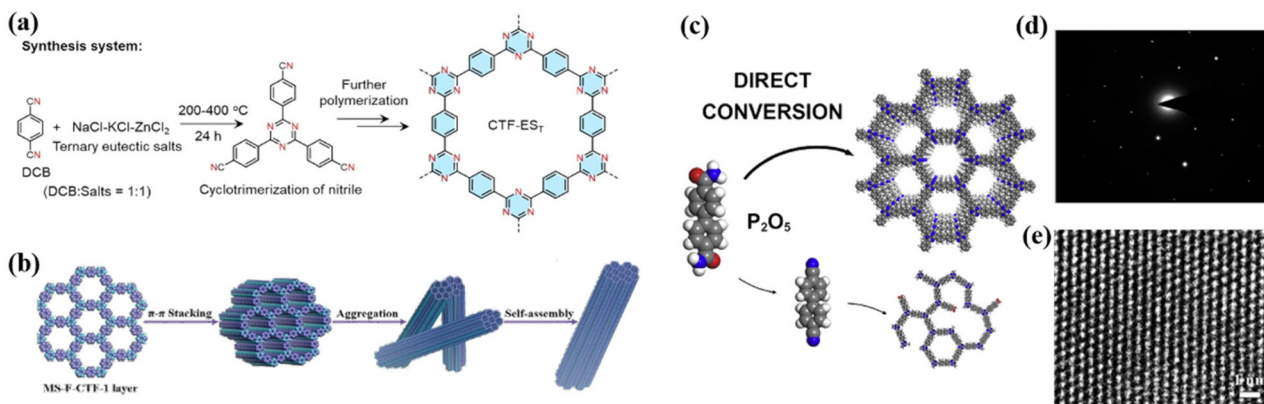


**Fig. 6** (a) Synthesis of CTF-ES<sub>T</sub> in ternary NaCl-KCl-ZnCl<sub>2</sub> eutectic salt system. Reproduced from ref. 86 with permission from Wiley-VCH, Copyright 2022. (b) Suggested mechanism for the formation of fiber for MS-F-CTF-1. Reproduced from ref. 91 with permission from Wiley-VCH, Copyright 2022. (c) Strategy of P<sub>2</sub>O<sub>5</sub>-assisted synthesis of CTFs. Reproduced from ref. 93 with permission from Elsevier, Copyright 2021. (d) Higher-magnification HR-TEM image and (e) SAED pattern of 2DP. Reproduced from ref. 96 with permission from the American Chemical Society, Copyright 2017.

black with an increase in temperature, indicating the carbonization of CTFs. The reason why the photocatalytic activity of CTFs decreased greatly with an increase in the polycondensation temperature may be that the increase in temperature led to more defects in CTFs. Therefore, the CTFs synthesized by ternary eutectic salt showed better crystallinity and photocatalytic performance.<sup>86</sup>

**2.3.2 Superacid-catalyzed strategy.** Under the assistance of a certain amount of superacid, the stacking mode of CTFs will generally change from the AB mode to AA mode, and this transformation in mode will eventually lead to CTFs with relatively high crystallinity, purity and specific surface area.<sup>87</sup> Liu *et al.* synthesized crystalline CTFs *via* the superacid-catalyzed strategy, in which 1,4-dicylidene was aggregated into CTFs *via* a trimer reaction in a CH<sub>2</sub>Cl<sub>2</sub>/CH<sub>3</sub>SO<sub>3</sub>H one-pot superacid catalyzed system.<sup>88</sup> Through detailed theoretical simulation, the obtained CTFs displayed a unique staggered AB stack configuration, and polarization microscope (POM) examination showed that the synthesized CTFs had a layered structure. More importantly, the yield of CTFs obtained using this superacid-catalyzed method can reach the gram level.

**2.3.3 In situ oxidation method.** The *in situ* oxidation method is based on the copolymerization reaction of aldehyde and amidine monomer using binary benzyl alcohol as the precursor, where the aldehyde monomer is slowly produced in the polymerization system, and compared with the above-mentioned method, this strategy does not use strong acid or high temperature and the reaction conditions are relatively mild. Wang *et al.* obtained layered CTF-HUST and CTF-HUSTs *via* the condensation reaction of aldehydes and amines in dimethyl sulfoxide,<sup>89</sup> but the crystallinity of these CTFs was low. Therefore, they improved on this method and found that the fiber morphology could be promoted by controlling the nucleation,<sup>90</sup> crystal growth, and self-assembly (Fig. 6b).<sup>91</sup> They found that controlling the nucleation rate of CTFs can also change their crystallinity, and alcohols can be oxidized to

aldehydes in dimethyl sulfoxide. Based on this, Liu and co-workers synthesized highly crystalline CTFs in an open system using the *in situ* alcohol oxidation method for the first time. This is also a general non-carbonization method, which slows down the nucleation process by controlling the *in situ* formation of the ethanol monomer.<sup>92</sup>

**2.3.4 Other methods.** In addition to the above-mentioned methods, several other strategies have been used to synthesize high-crystalline CTFs. Crystalline CTFs can also be synthesized under the catalysis of phosphorus pentoxide (P<sub>2</sub>O<sub>5</sub>) (Fig. 6c).<sup>93</sup> For example, Yu *et al.* proposed a strategy for the synthesis of CTFs using P<sub>2</sub>O<sub>5</sub> as the catalyst. In this process, CTFs were synthesized *via* the condensation of an aromatic primary amide group [C(=O)-NH<sub>2</sub>] into an s-triazine ring under P<sub>2</sub>O<sub>5</sub> catalysis.<sup>94</sup> The resulting CTFs also exhibited good crystallinity.

#### 2.4 Other crystalline polymeric materials

Besides the above-mentioned three high-crystalline g-C<sub>3</sub>N<sub>4</sub>, COFs and CTFs, there are some other highly crystalline organic polymeric catalysts. For instance, Chu *et al.* developed a crystalline polyimide photocatalyst by polymerizing melamine (MA) with pyromellitic dianhydride (PMDA), which exhibited excellent photocatalytic activity under visible light.<sup>95</sup> Liu *et al.* synthesized a two-dimensional triazine crystal polymer (2DP) (Fig. 6d and e) *via* the trimerization reaction of carbonitrile catalyzed by trifluoromethanesulfonic acid.<sup>96</sup>

### 3. Advantages of high-crystalline conjugated organic polymeric materials

Conjugated organic polymeric materials are good visible light-responsive photocatalysts, which exhibit structural diversity and functional tunability; however, their intrinsic stability and

photocatalytic activity are largely limited by their traditional amorphous or weakly crystalline structures,<sup>81,97</sup> together with abundant structural defects or trapping centers for the recombination of photogenerated electron-hole ( $e^-$ - $h^+$ ) pairs.<sup>98</sup> Therefore, the crystallinity of organic photocatalysts is critical for their improved stability and catalytic activity, which can be used to effectively regulate their electronic structures in various ways, and further used to measure their degree of ordered arrangement in the solid state. Some of the advantages of high crystallinity in conjugated organic polymeric materials are summarized below.

### 3.1 Reduces the concentration of defects

Plenty of defects will be introduced during the thermal polymerization process of precursors to prepare organic polymeric photocatalysts,<sup>99,100</sup> which is the pivotal factor leading to the random migration and rapid recombination of carriers,<sup>101</sup> resulting in an unsatisfactory photocatalytic effect. According to the literature, most conjugated organic polymeric materials (e.g., g-C<sub>3</sub>N<sub>4</sub>, COFs and CTFs) are low-crystalline or amorphous with many defects, which act as charge trap sites or charge recombination centers, leading to inhibited photocatalytic activities.<sup>38</sup> In this regard, constructing the relevant high-crystalline materials to eliminate the defects of charge trapping sites is an important approach to improve the charge transport and inhibit photogenerated charge recombination,<sup>38</sup>

which are critical factors to enhance the photocatalytic performance, especially for the photoreduction of CO<sub>2</sub>.

As shown in Fig. 7, a series of characterization methods was used to verify the presence of defects or vacancies in materials, such as X-ray absorption fine structure (XAFS) (Fig. 7a),<sup>102</sup> X-ray photoelectron spectroscopy (XPS) (Fig. 7b),<sup>103</sup> Raman spectroscopy (Fig. 7c),<sup>104</sup> scanning transmission electron microscopy (STEM) (Fig. 7d),<sup>105</sup> electron paramagnetic resonance spectroscopy (EPR) (Fig. 7e),<sup>57</sup> and positron annihilation lifetime spectroscopy (PALS) (Fig. 7f).<sup>106</sup> Specifically, XAFS can be employed to determine the defect levels by observing the migration distances between adjacent coordinating atoms and their peak intensities.<sup>107</sup> However, defects in materials can change their bonding energy, which can be observed in shifted peaks or emerging peaks. Therefore, XPS is also an effective method to detect the defect sites in materials.<sup>108</sup> Similarly, different chemical bonds exhibit different vibration modes, and a variation in the molecular vibration level causes a Raman shift. The presence of defects in materials can affect the vibration mode, leading to Raman shifts or new peaks.<sup>109</sup> STEM can be employed to observe the atomic number in the crystal structure and the way each atom is arranged and find defects in materials.<sup>110</sup> PALS is based on the positron lifetime to determine the defect type and the relative concentration of defects.<sup>111</sup> Among them, EPR technology is a relatively convenient and fast detection way for the detection of defects,

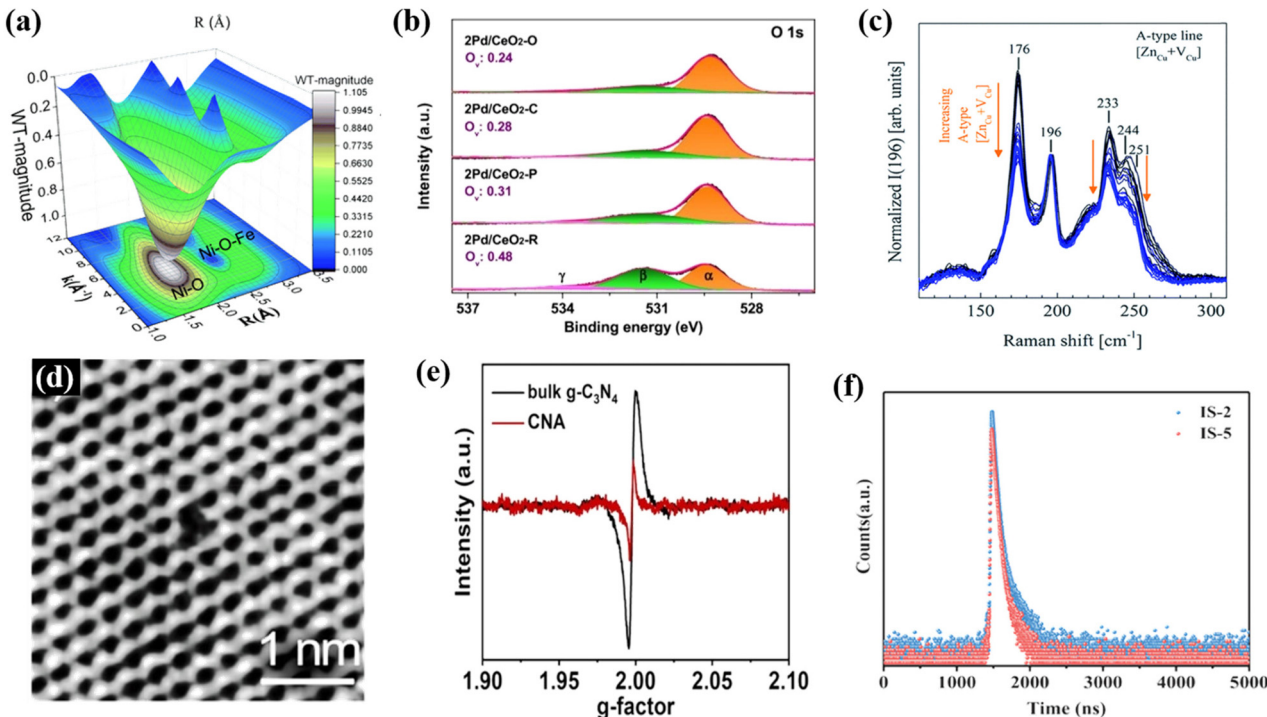


Fig. 7 Results from the methods used to characterize defects or vacancies: (a) XAFS. Reproduced from ref. 102 with permission from The Royal Society of Chemistry, Copyright 2021. (b) XPS. Reproduced from ref. 103 with permission from the American Chemical Society, Copyright 2020. (c) Raman spectra. Reproduced from ref. 104 with permission from The Royal Society of Chemistry, Copyright 2019. (d) STEM. Reproduced from ref. 105 with permission from the American Chemical Society, Copyright 2019. (e) EPR. Reproduced from ref. 57 with permission from Elsevier, Copyright 2022. (f) PALS. Reproduced from ref. 106 with permission from Wiley-VCH, Copyright 2022.

which can be judged according to the signal of the g factor in the Lorentzian line (at about 2.00) of unpaired electrons on the surface of materials.<sup>112</sup> Many reports on the defects of highly crystalline materials have employed EPR.<sup>47,62</sup> For example, in the recent work by our group, EPR was used to test the defects of the prepared catalysts. As shown in Fig. 7e through the EPR test, it can be concluded that the EPR signal intensity of the prepared highly crystalline carbon nitride (CNA) is low because the regulation of high crystallization eliminates the deep trapping sites of  $g\text{-C}_3\text{N}_4$ , and this low defect density also makes the catalyst have better ability to inhibit photogenerated electron–hole pair recombination and promote electron transfer.<sup>57</sup> In addition to the improvement in crystallinity in  $g\text{-C}_3\text{N}_4$ , the improvement in crystallinity in other organic polymeric materials can also improve the defect situation. For instance, Khan *et al.* developed a “liquid–gas phase-switching method” to synthesize COF films, and the resulting COF films had high crystallinity and a dense surface without defects. Compared with the initial COF films, the surface defects also disappeared after the crystallinity increased.<sup>113</sup> All these results indicate the merits of high-crystalline materials to eliminate defects.

### 3.2 Enhances the built-in electric field

A built-in-electric field in photocatalysts can drive the separation and migration of photogenerated  $e^-$ – $h^+$  pairs to the surface of photocatalysts.<sup>114,115</sup> Achieving a strong built-in electric field depends on two properties, as follows: (1) a high degree of crystallinity is necessary to obtain highly ordered structures and (2) the molecular dipole guarantees the ability of photogenerated charge separation. Therefore, the photocatalytic performance is closely related to the strength of the built-in-electric field. For instance, Zhang *et al.*<sup>116</sup> synthesized a high-crystalline perylene imide polymer photocatalyst (urea-

PDI). The advantages of high crystallinity and large dipole structure are conducive to the formation of a strong built-in electric field, making it possible for urea-PDI to have good charge separation and transport ability. Compared with other synthesized polymers (*e.g.*, hydrazine-PDI and ethylenediamine-PDI), urea-PDI exhibited superior crystallinity, which ensures the stable existence of an internal dipole-induced electric field in polymers. Fig. 8a shows the process of charge transfer under the action of an internal electric field in Li's report, according to the built-in electric field characterization,<sup>117</sup> where the surface charge density and zeta potential of urea-PDI were measured by atomic force microscopy with a Kelvin probe (KPFM), which can be used to index the built-in electric field. The results in Fig. 8b and c show that the surface potential and zeta potential of urea-PDI were much higher than that of other relevant catalysts, indicated its stronger built-in electric field with significantly enhanced charge separation and transportation, and it was further inferred that the high crystallinity allows the catalyst molecules to be arranged in an oriented space to provide channels for the rapid transfer of photogenerated charges. This conclusion was also confirmed in the report by Zhang *et al.*,<sup>40</sup> where the highly crystalline triazine-PDI achieved a remarkable photocatalytic performance due to the enhanced built-in electric field. Recently, Guo *et al.*<sup>118</sup> reported that a carbon nitride homogeneous junction (triple-crystallinity) with different crystallinity induced a high-efficiency photocatalytic performance due to the electric field enhancement at the interface. The results showed that the increase in crystallinity led to a decrease in the Fermi level and band position, resulting in the band bending of space charge region and interface, which in turn created a built-in electric field. As shown in Fig. 8d and e, the difference in electron density was used to analyze the built-in electric field of tri-crystallinity carbon nitride (CN) after photoexcitation,

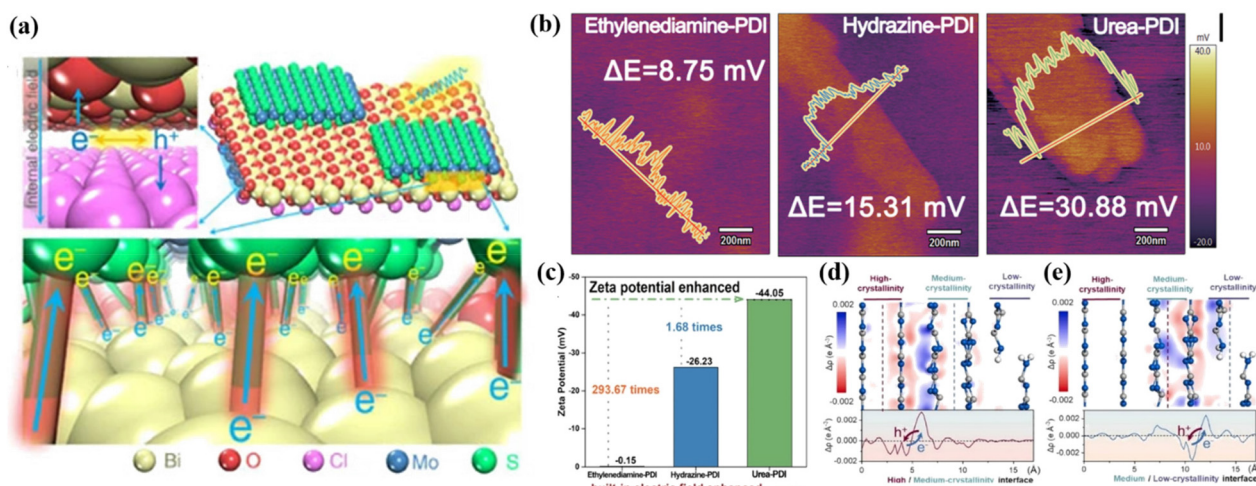


Fig. 8 (a) Charge transfer process at the interface. Reproduced from ref. 117 with permission from Springer Nature, Copyright 2016. (b) Surface potential of different polymers detected with KPFM. Reproduced from ref. 116 with permission from Wiley-VCH, Copyright 2020. (c) Zeta potential of different polymers. Reproduced from ref. 116 with permission from Wiley-VCH, Copyright 2020. (d) High/medium-crystallinity interface and (e) medium/low-crystallinity interface. Reproduced from ref. 118 with permission from Elsevier, Copyright 2022.

where more photogenerated holes were accumulated at high and medium crystallinity CN at the interface of high/medium and medium/low crystallinity CN, respectively. These charge accumulation characteristics also confirmed the existence and direction of the built-in electric field. The built-in electric field improved the charge separation and transfer efficiency, and thus its photocatalytic efficiency is much higher than that of the general  $\text{g-C}_3\text{N}_4$ . The advantages of high crystallinity to achieve an internal electric field are also reflected in other conjugated organic polymeric materials. For example, the amorphous  $\text{g-C}_3\text{N}_4$  with nitrogen vacancy ( $\text{g-C}_3\text{N}_4(\text{NH})$ ) synthesized by Wang *et al.*<sup>119</sup> and the crystalline COF (TP-TTA COF), which was easily deposited on  $\text{g-C}_3\text{N}_4(\text{NH})$ , formed a heterojunction through  $\pi$ - $\pi$  interaction, leading to the formation of a strong built-in electric field. This is beneficial for the separation of charge carriers in the  $\text{g-C}_3\text{N}_4(\text{NH})$ /COF photocatalytic reaction, thus improving the catalytic performance.

### 3.3 Reduces interlayer hydrogen bonds

Usually, there are abundant interlayer hydrogen bonds in conjugated organic polymeric materials; however, interlayer hydrogen bonds act as channels for charge transport and recombination in photocatalytic reactions, and excess interlayer hydrogen bonds will greatly limit the specific surface area and active sites, thereby inhibiting the catalytic efficiency. Iqbal *et al.* found that the interlayer hydrogen bonds can be broken by preparing high-crystalline  $\text{g-C}_3\text{N}_4$  *via* a two-step heat treatment process. Compared with the usual bulk  $\text{g-C}_3\text{N}_4$ , highly crystalline  $\text{g-C}_3\text{N}_4$  possess significantly decreased interlayer hydrogen bonds and ordered  $\pi$  conjugate system, which is conducive to realizing a high efficiency separation and suppressed recombination of photogenerated  $e^-$ - $h^+$  pairs, leading to a drastic improvement in photocatalytic activity.<sup>41</sup> Therefore, high-crystalline materials can effectively reduce the interlayer hydrogen bonds, thereby promoting the photocatalytic activity.

In addition, Kandambeth *et al.* found that construction of appropriate intramolecular hydrogen bonds also realized the transition of COFs from amorphous to crystalline state, and promoted a transition from disordered to ordered skeleton.<sup>72</sup> Hydrogen bonds can also lock the molecular structure of COF materials and improve their planarity, thus further increasing their crystallinity.

### 3.4 Crystal plane regulation

It is well known that the crystal plane of semiconductors greatly affects their catalytic activities, where different crystal planes exhibit different electronic structures and surface reaction performances. Thus, crystal plane regulation is crucial for improving the photocatalytic performance. However, the general conjugated organic polymeric materials prepared *via* the conventional thermal polymerization methods possess low crystallinity and instability, which impede the understanding of the atomic structure and the identification of the role of the reaction surface role in promoting photocatalytic reactions on materials.

The construction of high-crystalline materials is an effective strategy to regulate their crystal planes. For example, Lin *et al.* prepared(PTIs)/ $\text{Li}^+\text{Cl}^-$  high-crystalline polytriazine imides with different crystal faces and different aspect ratios *via* an ion-thermal method for photocatalytic overall water splitting. As shown in Fig. 9a, all the crystals form prismatic crystals surrounded by two hexagonal  $\{0001\}$  planes as base planes and six rectangular prismatic planes  $\{10\bar{1}0\}$ . The aberration-corrected integrated differential phase contrast (AC-iDPC) image (Fig. 9b-d) showed the highly ordered atomic structure of PTI/ $\text{Li}^+\text{Cl}^-$ . Some *in situ* experimental characterizations and theoretical calculations showed that the  $\{10\bar{1}0\}$  plane is beneficial for electron transfer and catalytic reaction, where its overall water splitting performance is linearly related to the relative surface area of the  $\{10\bar{1}0\}$  and  $\{0001\}$  planes.<sup>39</sup> Therefore, the construction of high-crystalline conjugated organic polymeric materials and screening the optimal crystal planes are efficient strategies for enhanced photocatalytic performance.

## 4. Modification of high-crystalline conjugated organic polymeric materials

High-crystalline conjugated organic polymeric materials are candidates for solar energy conversion due to their various advantages; however, their photocatalytic performance is still limited due to their limited visible light response and electron transfer efficiency. Thus, to further improve their photocatalytic efficiency, various modification strategies have been

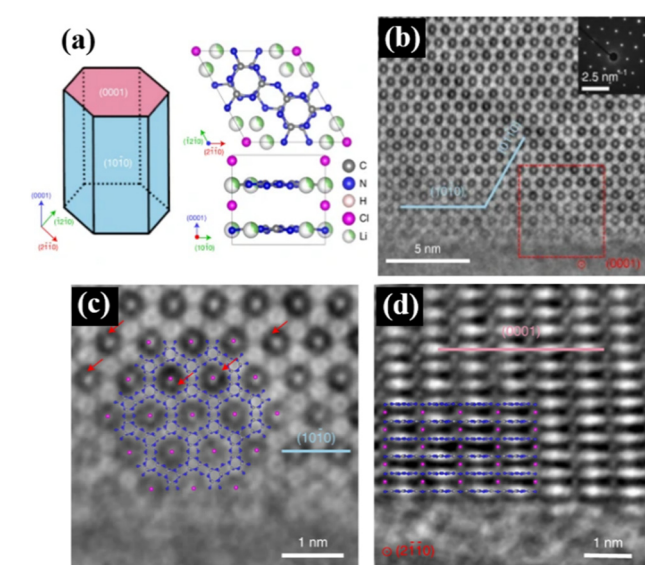


Fig. 9 (a) Left, schematic illustration of the PTI/ $\text{Li}^+\text{Cl}^-$  crystal. Right, crystal structure of PTI/ $\text{Li}^+\text{Cl}^-$ . (b) AC-iDPC images of a typical PTI/ $\text{Li}^+\text{Cl}^-$  crystal. The inset shows the corresponding diffraction pattern. (c) Expanded view of the red box in (b). (d) AC-iDPC images of a typical PTI/ $\text{Li}^+\text{Cl}^-$  crystal aligned along the  $(21\bar{1}0)$  direction. Reproduced from ref. 39 with permission from Springer Nature, Copyright 2020.

developed, such as defect engineering, element doping, surface loading, and construction of heterojunctions.

#### 4.1 Defect engineering

Improving the crystallinity and introducing defects are two effective ways to ameliorate the photocatalytic activities of conjugated organic polymeric materials, but these two methods are inherently contradictory. As mentioned above herein, high crystallinity may lead to a decrease in surface defects in catalysts; nevertheless, the introduction of defects can lead to a decrease in the crystallinity of materials. Therefore, it is necessary to balance the crystallinity and defects in organic catalysts. Photocatalysts can only possess excellent catalytic activity when they have an appropriate amount of defects, while maintaining high crystallinity.

Some works have been devoted to this research. For instance, Ren *et al.* introduced some additional groups to promote the dissociation of excitons and inhibit the recombination of photogenic  $e^- - h^+$  pairs. Cyanogen defects were introduced in the polymer backbone without affecting the crystallinity (Fig. 10a and b), which enhanced the light absorption capacity, accelerated the charge separation, and enhanced the photocatalytic performance.<sup>120-122</sup>

The reasonable introduction of vacancies can serve as additional active sites to facilitate photocatalytic reactions, and excitons can accelerate dissociation near the defect sites. As shown in Fig. 10c, Liu *et al.* reported a facile alkali-assisted molten salt method to prepare nitrogen-vacancy-rich crystalline  $g\text{-C}_3\text{N}_4$ , in which LiCl/KCl was used to obtain crystalline CN to enhance the crystallinity, and potassium hydroxide was used to remove some nitrogen atoms *in situ* to generate nitrogen vacancies.<sup>123</sup> The HRTEM results, as shown in Fig. 10d,

indicated that the polymer still retained high crystallinity after introducing nitrogen defects.

#### 4.2 Element doping

Heteroatom doping is a well-known and effective way to improve the photocatalytic performance of materials, and it is a simple and valid method to adjust the light absorption, electronic structure and band gap of catalysts. This includes metal doping (e.g., Ni, Cu, and Co),<sup>124,125</sup> alkaline earth metal doping (e.g., K and Na),<sup>61</sup> and non-metal doping (e.g., C, B, F, and Cl).<sup>126</sup> For instance, Zhang *et al.* synthesized a series of highly crystalline  $g\text{-C}_3\text{N}_4$  with K intercalation by a molten salt method using melamine as the precursor. The intercalation of K element regulated the surface active sites on the  $g\text{-C}_3\text{N}_4$  framework and greatly improved the photocatalytic activity. Li *et al.* inserted Cl element into the intermediate layer of CTF-1 through a covalent bridge by ball-milling stripping-assisted acidification (Fig. 11a), resulting in a unique electronic structured COF(Cl-ECF). In this Cl-ECF, a covalent interlayer channel of Cl-C and Cl-N covalent bond was formed, which promoted the electron delocalization and separation and migration of carriers. In addition, the insertion of Cl element can narrow the band gap of Cl-ECF, which can effectively activate more photoinduced charge carriers, thereby improving the photocatalytic performance.<sup>128</sup> Zhu *et al.* prepared a series of P-, S-, Se-doped CTF-1 by high-temperature annealing (Fig. 11b), in which a built-in electric field was generated by the spin polarization, resulting in the promoted separation and transfer of  $e^- - h^+$  pairs, which greatly improved the photocatalytic efficiency.<sup>129</sup> Chen *et al.* prepared K<sup>+</sup>, Ni- and N-doped crystalline  $g\text{-C}_3\text{N}_4$  by Ni<sup>2+</sup> anchoring and the supramolecular thermal polymerization of encapsulated melamine-cyanic acid, and then recalcination in a mixture of KCl/LiCl. The obtained strip-like K<sup>+</sup>, Ni and C co-doped crystalline  $g\text{-C}_3\text{N}_4$  displayed excellent charge separation efficiency, light absorption capability, and photoreduction ability.<sup>130</sup> It can be seen that element doping is an effective method to improve the photocatalytic performance of high-crystalline  $g\text{-C}_3\text{N}_4$ .

More interestingly, element doping and defect engineering can synergistically regulate the electronic structure of catalysts, which can more effectively enhance their visible light absorption, promote charge separation, and capture more useful electrons to participate in surface reactions.<sup>131</sup> For example, Zhang *et al.* realized the construction of K-doped together with cyanide-defected crystalline  $g\text{-C}_3\text{N}_4$  using KCl as a template. In this process, K<sup>+</sup> ions were doped gradually into heptazine-based CCN (KCCN) by controlling their diffusion rates from surface to body (Fig. 11c and d), resulting in gradient changes in the electronic structure, band position and band gap in the same crystalline  $g\text{-C}_3\text{N}_4$ .<sup>132</sup> The high crystallinity of this bifunctional  $g\text{-C}_3\text{N}_4$  can be demonstrated by its clear lattice fringes in the HRTEM image (Fig. 11e). More importantly, the K<sup>+</sup> concentration gradient and newly formed cyanide defects can induce a built-in electric field, which greatly facilitates exciton dissociation, charge transport and separation. Wu *et al.*<sup>133</sup> also obtained a bifunctional crystalline  $g\text{-C}_3\text{N}_4$  catalyst (ACNN) with

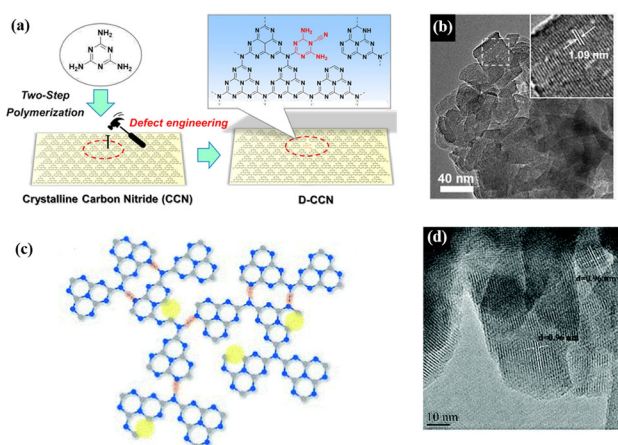


**Fig. 10** (a) Illustration of the defect engineering strategy. Reproduced from ref. 120 with permission from Wiley-VCH, Copyright 2019. (b) TEM images of D-CCN. Reproduced from ref. 120 with permission from Wiley-VCH, Copyright 2019. (c) Proposed structure of CN-NVs-CTe (nitrogen vacancies are marked by yellow circles). Reproduced from ref. 123 with permission from The Royal Society of Chemistry, Copyright 2020. (d) HRTEM image of CN-NVs-CTe. Reproduced from ref. 123 with permission from The Royal Society of Chemistry, Copyright 2020.

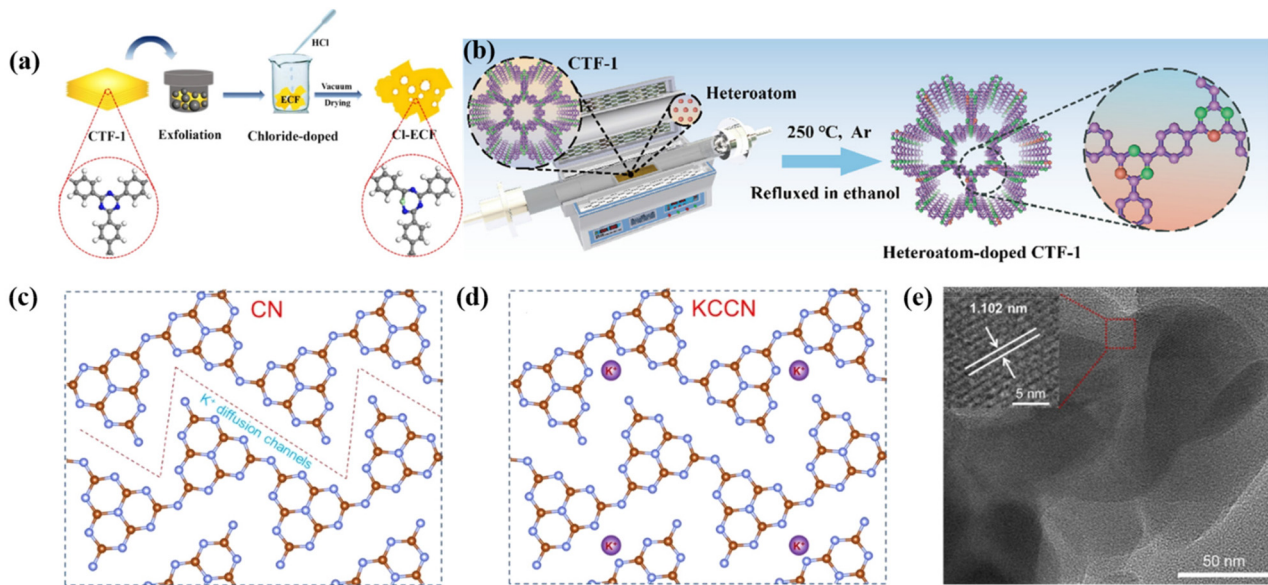


**Fig. 11** (a) Schematic diagram of the preparation for Cl-ECF photocatalysts. Reproduced from ref. 128 with permission from Elsevier, Copyright 2020. (b) Schematic illustration of the synthetic process of HA-CTF-1. Reproduced from ref. 129 with permission from the American Chemical Society, Copyright 2022. Proposed molecular structure for (c) CN and (d) KCCN. Reproduced from ref. 132 with permission from the American Chemical Society, Copyright 2021. (e) HRTEM image of KCCN. Reproduced from ref. 132 with permission from the American Chemical Society, Copyright 2021.

both alkali metal doping and N vacancies *via* a molten salt method. This bifunctional ACNN successfully expanded the visible light absorption range, suppressed charge recombination, and reduced the band gap from 2.85 to 2.63 eV. Thus, this synergistic effect of element doping and defect engineering has good prospects in improving the utilization of photo-generated charges and promoting photocatalytic reactions.

#### 4.3. Surface loading

Conjugated organic polymeric materials are also good carriers with abundant tunable sites and specific geometric and electronic structures, which are suitable for the loading of a cocatalyst or grafting of organic molecules to enhance their catalytic activities. In recent years, surface-modified catalysts with single atoms have developed rapidly and attracted attention from many researchers because a single metal can maximize the utilization of catalytic sites and form strong interactions with carriers to promote the catalytic efficiency. Li *et al.* synthesized a CTF-PDDA-TPDH catalyst by stabilizing Pt single atoms (SA) in the N<sub>3</sub> sites of ultrathin CTF nanosheets. DFT calculation showed that the single Pt atom was anchored by the -N<sub>3</sub> site (Fig. 12a), and the Pt-N<sub>3</sub> coordination structure also became the photocatalytic active site. The wavelet transform extended X-ray absorption fine structure (WT-EXAFS) diagram (Fig. 12b) confirmed that Pt existed in the catalyst as a single atom. The photogenerated electrons in the conduction band of CTF could be quickly transferred to Pt single atoms, and further facilitated the separation and transfer of charges.<sup>134</sup> Huang *et al.* used the special geometric and electronic structure of CTF-1 to prepare a Co-SA/CTF (Co-SA/CTF)

catalyst through the space constraint effect and coordination interaction for photocatalytic CO<sub>2</sub> reduction. The introduction of Co single atoms not only enhanced the adsorption of CO<sub>2</sub>, but also accelerated the separation and transfer of photocarriers, thereby promoting the photocatalytic performance.<sup>135</sup> Shen and co-workers reported a one-step method for the synthesis of single-atom molten Co salt coordinated with a crystalline g-C<sub>3</sub>N<sub>4</sub>/PTI heterojunction based on the built-in electric field in a homogeneous junction, which facilitates charge separation and single-atom loading for accelerating surface catalytic kinetics. The WT-EXAFS (Fig. 12c) analysis confirmed the existence of single-atom Co. Therefore, while improving the crystallinity, the charge transfer was promoted by adjusting the electronic structure of the Co single atom to achieve high-efficiency photocatalytic performances.<sup>124</sup>

Another surface-loading strategy is to graft organic molecules with excellent photocatalytic properties on the surface of g-C<sub>3</sub>N<sub>4</sub> to construct an electron donor-acceptor (D-A) structure. Our team reported the grafting of a high-crystalline g-C<sub>3</sub>N<sub>4</sub> nanoarray (CNA) of the organic small molecule perylene tetracarboxylic dianhydride (PTCDA) to build a D-A structure to improve the visible light response of the catalyst (Fig. 12d). Consequently, this accelerated the charge transport and promoted the separation of redox centers, namely electronic PTCDA molecular absorption and pyridine N atoms can be used as the reduction center and seven oxazine units as the oxidation site.<sup>57</sup> Thus, high crystallization eliminates defects in the material and prevents rapid charge reorganization, while the D-A structure enables the separation of redox centers to facilitate the photocatalytic hydrogen peroxide

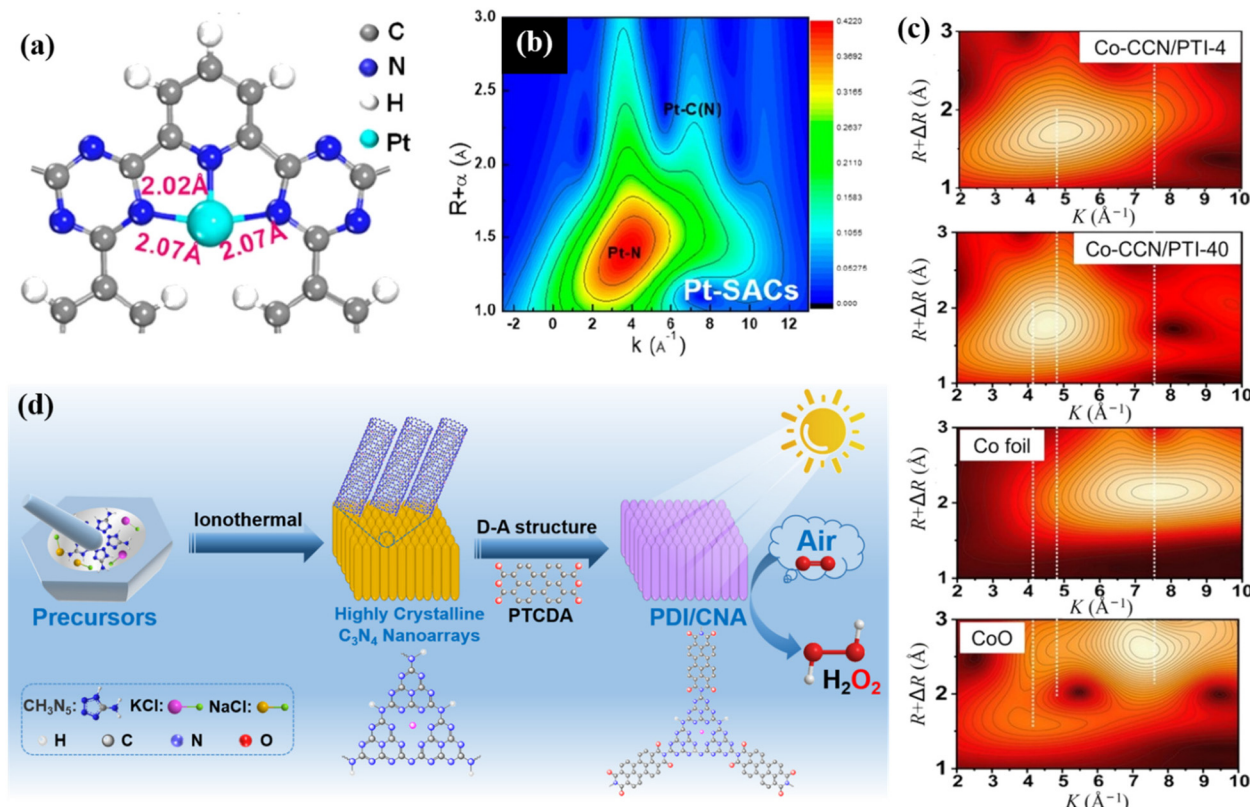


**Fig. 12** (a) DFT-optimized structure of the Pt-SACs/CTF catalyst. Reproduced from ref. 134 with permission from the American Chemical Society, Copyright 2020. (b) WT-EXAFS of Pt-SACs/CTF. Reproduced from ref. 134 with permission from the American Chemical Society, Copyright 2020. (c) Topographical maps of WT-EXAFS of Co-CCN/PTI-4 and Co-CCN/PTI-40. Reproduced from ref. 124 with permission from Science China Press, Copyright 2021. (d) Schematic illustration of PDI/CNA catalyst fabrication. Reproduced from ref. 57 with permission from Elsevier, Copyright 2022.

(H<sub>2</sub>O<sub>2</sub>) synthesis process. In addition, while ensuring crystallinity, many small molecular materials and functional groups have been used to modify conjugated organic polymers to improve their catalytic performance, such as cyclized quaternary ammonium bipyridine molecules,<sup>136</sup> polyethylene glycol,<sup>137</sup> and acetylene (–C≡C–) and diacetylene (–C≡C–C≡C–) moieties.<sup>138</sup> This strategy of surface loading is one of the effective methods to improve the properties of conjugated organic polymeric materials.

#### 4.4 Construction of heterojunctions

The construction of semiconductor heterojunctions is also one of the most common and effective methods to improve the catalyst efficiency, and thus is widely used in the design of catalysts.<sup>15,139</sup> The photocatalytic mechanisms of heterojunctions generally include type-I, type-II, Z-scheme, and S-scheme, which can improve the catalytic activity from different angles. The main purpose of constructing heterojunctions is to regulate the redox potential, enhance the visible light response, accelerate the separation of carriers, and promote the transfer and migration of photogenerated charges through the formed built-in electric field at the hetero-interface and effectively suppresses their recombination, thereby facilitating the photocatalytic effect.

The charge transfer mode, advantages and disadvantages of different heterostructures are also different. In the type-I heterojunction, both the VB and CB edges of one semiconductor are aligned to the band gap of the other half of the conductor, forming a straddle alignment. Although efficient photocatalytic activity exists in the type-I heterojunction, the photo-generated electrons and holes of the semiconductor may be transferred to the other half of the conductor, leading to electron hole pair recombination. In type-II semiconductor heterojunctions, the CB and VB are higher than the other half conductor and the chemical potential difference between them makes the band bending result in the formation of a built-in electric field. This promotes the movement of the photoproduced electron-hole pairs in opposite directions, leading to different heterojunction side electron-hole space separation.<sup>140</sup> Considering the shortcomings of type-II charge transfer from a thermodynamic point of view, improving the charge separation efficiency is achieved by sacrificing the redox ability, and from a kinetic point of view, the existence of an electrostatic effect will also make the original e<sup>–</sup>–h<sup>+</sup> in the photocatalyst inhibit the transfer of electron holes in other catalysts, which is not conducive to the photocatalytic reaction.<sup>141</sup> The advantage of the Z-scheme heterojunction is that it has one photocatalyst with strong reducing electrons and another

photocatalyst with strong oxidizing holes. However, the traditional Z-scheme heterojunction is limited to reacting only in an aqueous environment. In the new Z-scheme heterojunction system, including all-solid Z-scheme heterojunction and direct Z-scheme heterojunction, this problem is alleviated, but the direction of electron hole transfer is still controversial.<sup>142</sup> S-scheme heterojunctions can realize the spatial separation of photogenerated  $e^-$  and  $h^+$  through the built-in electric field, band bending and electrostatic effect.<sup>143</sup> Therefore, the construction of suitable heterojunction catalysts is still a promising means to improve the photocatalytic reactivity.

Our group obtained highly crystalline  $\text{g-C}_3\text{N}_4$  (CCN) and  $\text{ReS}_2$  *via* a template-mediated method and solvent stripping method, respectively. The  $\text{ReS}_2$  and CCN heterojunction was obtained *via* self-assembly. As shown in Fig. 13a, the photo-generated electrons on the CB of CCN would be transferred to  $\text{ReS}_2$ , and the accumulated electrons would be used for photocatalytic reduction reaction. High crystallinity and heterogeneous interfaces contribute to photogenerated carrier migration, and thus enhance the catalytic activity.<sup>63</sup> Lin *et al.* achieved a good photocatalytic performance using a CCN/LaOCl heterojunction *via* the *in situ* growth of highly crystalline  $\text{g-C}_3\text{N}_4$  on the surface of LaOCl. The high crystallinity of  $\text{g-C}_3\text{N}_4$  is favorable for the transport of photoexcited charges, and the built-in electric field formed at the hetero-interface can promote the separation of excited electron-holes, thereby inhibiting their recombination, and finally achieving a good photocatalytic performance.<sup>146</sup> In addition, the heterojunctions with different crystal phases of the same material can remarkably eliminate the interfacial defects.<sup>144,147,148</sup> The

built-in electric field formed by this close contact heterogeneous interface (Fig. 13b) and improved crystallinity make the catalyst much better. He *et al.* constructed a metal-free CN/CTF heterojunction by combining CTF and  $\text{g-C}_3\text{N}_4$  through a simple self-assembly method. The addition of highly crystalline CTF greatly promoted the photocatalytic activity of  $\text{g-C}_3\text{N}_4$  due to the stable structure of the CTF crystal.<sup>145</sup> This metal-free CN/CTF heterojunction exhibited excellent photocatalytic  $\text{CO}_2$  reduction activity due to the hetero-interface effect (Fig. 13c). Furthermore, Xu *et al.* synthesized a covalent organic framework-based (P-COF-1)/CTF heterojunction with a 2D-2D heterojunction structure through intermolecular  $\pi$ - $\pi$  interaction. The construction of COF and CTF heterojunctions increases the visible light absorption and the separation efficiency of photogenerated carriers.<sup>149</sup> Cheng *et al.* prepared a heterojunction photocatalyst for the directional charge movement of an S-scheme heterojunction by anchoring single-atom Co to  $\text{CeO}_2$  and by introducing it in highly crystalline  $\text{g-C}_3\text{N}_4$  (named CeCo-PTI). The efficient and selective photocatalytic reduction of  $\text{CO}_2$  to methane was achieved through the site regulation of the directed charge transfer of this special S-scheme heterojunction.<sup>150</sup>

## 5. Application in photocatalytic $\text{CO}_2$ reduction

Carbon dioxide conversion is an effective way to convert this waste carbon source into renewable energy *via* low-carbon sustainable development strategies, including thermochemical catalysis,<sup>151</sup> electrochemical reduction,<sup>152</sup> biological catalysis,<sup>153</sup> photoelectric chemical catalysis<sup>154</sup> and photocatalytic reduction.<sup>155</sup> Among them, photocatalytic  $\text{CO}_2$  reduction is an extremely promising route. It is well known that a typical semiconductor photocatalytic  $\text{CO}_2$  reduction process involves the five steps, as follows: light absorption, charge separation,  $\text{CO}_2$  adsorption, surface redox reaction, and product desorption, which are all critical for efficient  $\text{CO}_2$  conversion. In this regard, high-crystalline conjugated organic polymeric materials (such as  $\text{g-C}_3\text{N}_4$ , COFs, and CTFs) exhibit remarkable photocatalytic  $\text{CO}_2$  conversion effects, and thus are attracting attention from researchers because of their advantages of tunable molecular or electronic structure, excellent visible light response, and unique properties of photocarrier separation and transport enabled by their  $\pi$  conjugated stacking structures. In this section, we separately introduce the application of different high-crystalline conjugated organic polymeric materials in photocatalytic  $\text{CO}_2$  reduction and their photocatalytic activities are summarized in Table 1.

### 5.1 Crystalline $\text{g-C}_3\text{N}_4$ for photocatalytic $\text{CO}_2$ reduction

The  $\text{g-C}_3\text{N}_4$  catalyst is a typical conjugated organic polymeric material and one of the most commonly used catalysts for the photocatalytic reduction of  $\text{CO}_2$ .<sup>165</sup> It is widely used in the field of photocatalysis due to its suitable CB position, metal-free inherent property, and good catalytic activity. However,

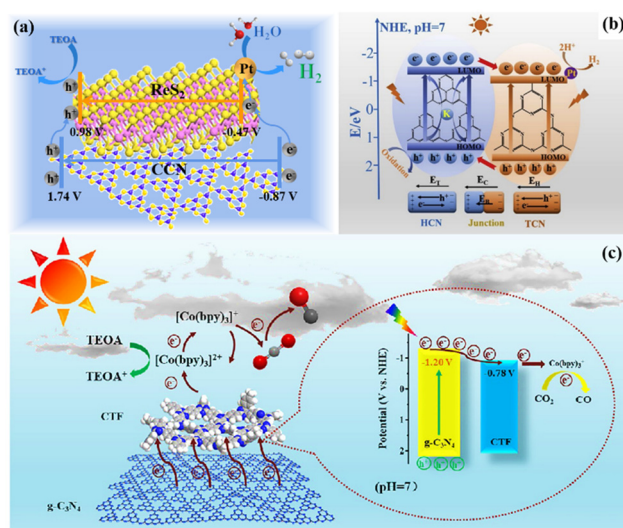


**Fig. 13** (a) 2D/2D  $\text{ReS}_2$ /CCN heterojunction. Reproduced from ref. 63 with permission from Elsevier, Copyright 2022. (b) Built-in electric field formed by the heterojunction. Reproduced from ref. 144 with permission from Elsevier, Copyright 2020. (c) Schematic mechanism of CN/CTF heterostructure for photocatalytic  $\text{CO}_2$  reduction. Reproduced from ref. 145 with permission from the Chinese Academy of Sciences, Copyright 2022.

**Table 1** Summary of the performance of photocatalytic  $\text{CO}_2$  conversion on high-crystalline organic polymeric materials

Photocatalyst	Light source	Products	Selectivity	Yield ( $\mu\text{mol g}^{-1} \text{h}^{-1}$ )	Ref.
Crystalline $\text{g-C}_3\text{N}_4$ based photocatalysts	CN-ATZ-NaK	350 W Xe lamp (AM1.5 filter) $\text{CO}, \text{CH}_4, \text{CH}_3\text{OH}$	CO	CO (14 $\mu\text{mol g}^{-1} \text{h}^{-1}$ )	156
	CNNA/rGO	350 W Xe lamp (AM1.5 filter) $\text{CH}_4, \text{CO}, \text{CH}_3\text{OH}, \text{C}_2\text{H}_5\text{OH}$	CO (64.6%)	CO (3.67 $\mu\text{mol g}^{-1} \text{h}^{-1}$ )	157
	Cu-CCN	300 W Xe lamp $\text{CO}$	CO (100%)	CO (3.086 $\mu\text{mol g}^{-1} \text{h}^{-1}$ )	158
	CeCo-PTI	350 W Xe lamp $\text{CO}, \text{CH}_4$	$\text{CH}_4$ (88.3%)	$\text{CH}_4$ (45.4 $\mu\text{mol g}^{-1} \text{h}^{-1}$ )	150
Crystalline COFs based photocatalysts	TTCOF-Zn	300 W Xe lamp $\text{CO}$	CO (100%)	CO (12.33 $\mu\text{mol}$ after 60 h)	159
	$\text{sp}^2\text{C-COF}$	300 W Xe lamp ( $\lambda \geq 420$ nm) $\text{CO}$	CO (84%)	CO (1040 $\mu\text{mol g}^{-1} \text{h}^{-1}$ over 17.5 h illumination)	160
	HBC-TFPN	300 W Xe lamp ( $\lambda \geq 420$ nm) $\text{CO}, \text{H}_2$	CO (92%)	CO (7.7 $\mu\text{mol g}^{-1} \text{h}^{-1}$ )	161
	TRITER-2	20 W white LED irradiation $\text{—}$	$\text{CH}_3\text{OH}$	—	162
	$\text{Pd}_{x}\text{In}_{y}@\text{N}_3\text{-COF}$	A 300 W Xe lamp (with a 400 nm filter) $\text{CH}_3\text{OH}, \text{CH}_3\text{CH}_2\text{OH}$	$\text{CH}_3\text{OH}$ (74%)	$\text{CH}_3\text{OH}$ (590.52 $\mu\text{mol g}^{-1}$ in 24 h)	71
Crystalline CTFs based photocatalysts	$\text{MCOF-Ti}_6\text{Cu}_3$	300 W Xe lamp (AM1.5 filter) $\text{—}$	$\text{HCOOH}$	$\text{HCOOH}$ (77.3 $\mu\text{mol g}^{-1} \text{h}^{-1}$ )	163
	PT-SA/CTF-1	300 W Xe lamp (with a 420 nm filter) $\text{CO}, \text{CH}_4$	CO	CO (4.5 $\mu\text{mol g}^{-1} \text{h}^{-1}$ )	164
	CN/CTF	300 W Xe lamp $\text{CO}$	CO (99.9%)	CO (151.1 $\mu\text{mol g}^{-1} \text{h}^{-1}$ )	145

the photocatalytic performance of general low-crystalline or amorphous  $\text{g-C}_3\text{N}_4$  is limited by its disordered electronic structure, low charge utilization, rapid recombination of carriers, and limited light absorption. More importantly, it is difficult to control the product selectivity of photocatalytic  $\text{CO}_2$  reduction with the general amorphous  $\text{g-C}_3\text{N}_4$ , often producing some complex mixtures, which makes the separation of products in practical applications challenging. In this case, crystalline  $\text{g-C}_3\text{N}_4$ -based photocatalysts exhibit excellent efficiency and high product selectivity in  $\text{CO}_2$  conversion due to their multiple advantages.

For example, Zhang *et al.* prepared crystalline  $\text{g-C}_3\text{N}_4$  by the molten salt method, which exhibited a significantly enhanced visible light response compared to the general amorphous  $\text{g-C}_3\text{N}_4$ . It exhibited excellent photocatalytic activity without the use of metal cocatalysts and sacrificial agents during  $\text{CO}_2$  conversion, the product was dominated by CO and the production rate is as high as about 14  $\mu\text{mol/g h}^{-1}$ , which is much higher than the currently reported  $\text{g-C}_3\text{N}_4$ -based materials.<sup>156</sup> The high-crystalline  $\text{g-C}_3\text{N}_4$  obtained by the molten salt method exhibited an excellent photocatalytic performance due to the enhanced light absorption and the improved  $\pi-\pi^*$  electronic transitions.

Compared with the research on the photocatalytic  $\text{CO}_2$  reduction with pristine crystalline  $\text{g-C}_3\text{N}_4$ , more research is devoted to further improving the photocatalytic activity of crystalline  $\text{g-C}_3\text{N}_4$  by some modification measures. While maintaining good crystallinity, introducing defects (such as cyanide group and vacancy) and ions<sup>125,166,167</sup> and constructing heterojunctions are efficient ways to promote the adsorption and activation of the  $\text{CO}_2$  molecule, and improve photoelectron transfer ability and utilization rate, thereby improving the  $\text{CO}_2$  reduction ability. As is shown in Fig. 14a, Xia *et al.* constructed a unique 2D/1D graphene/polyheptazinimide heterojunction (denoted as CNNA/rGO). Fig. 14b shows the ordered 1D crystalline carbon nitride nanorod crystal structure, which provides a pathway for light harvesting to achieve a fast reduction process and a direct path for photoelectron transfer to the graphene

surface, improving the light absorption and interfacial charge transfer. The total  $\text{CO}_2$  conversion achieved was 12.63  $\mu\text{mol g}^{-1} \text{h}^{-1}$  without the addition of a cocatalyst and sacrificial agent.<sup>157</sup>

The main product is CO, but an interesting phenomenon is that the increase in crystallinity makes the content of  $\text{C}_2\text{H}_5\text{OH}$  in the product increase, which may be because the introduction of rGO helps to accumulate photogenerated charges and improve the adsorption of  $\text{CO}_2$ .  $\text{C}_2\text{H}_5\text{OH}$  is produced through the coupling of the intermediate methoxyl ( $\text{OCH}_3$ ) and methyl ( $\text{CH}_3$ ) radicals. The obtained composite catalyst with crystalline microstructure significantly improved the light absorption, exciton splitting, charge transport, and selective  $\text{CO}_2$  binding, resulting in the efficient photoreduction of  $\text{CO}_2$  to chemical fuel.<sup>157</sup> In addition, as shown in Fig. 14c, Li *et al.* supported a Cu single atom on crystalline  $\text{g-C}_3\text{N}_4$  (Cu-CCN) based on the molten salt method and reflow method to improve the photocatalytic  $\text{CO}_2$  reduction performance. The presence of excessive defects in amorphous  $\text{g-C}_3\text{N}_4$  limits the enhancement in catalytic activity with the introduction of single atoms. Thus, it is a good strategy to replace amorphous  $\text{g-C}_3\text{N}_4$  with crystalline  $\text{g-C}_3\text{N}_4$ . Here, Cu atoms can provide sites for  $\text{CO}_2$  activation. *In situ* Fourier transform infrared spectroscopy (ISFTIR) (Fig. 14d and e) was used to accurately detect the  $\text{CO}_2$  reduction process and to determine the reaction mechanism by capturing the intermediates. The results showed that the  $\text{CO}_2$  molecule was absorbed on the surface of Cu-CCN samples in the form of  $\text{HCO}_3^-$ , and the main intermediate in this  $\text{CO}_2$  reduction process was  $\text{HCOO}^-$ . Furthermore, DFT theoretical simulation calculations (Fig. 14f) showed that the  $\text{CO}_2$  adsorbed on the Cu-CCN samples initially generated  $^*\text{HCOO}$ , which was then converted to  $^*\text{CO}$  and  $^*\text{CHO}$ . In this process, the transition from  $^*\text{HCOO}$  to  $^*\text{CO}$  is more thermally advantageous, and thus it is easier for this process to reduce  $\text{CO}_2$  to CO. Combined with the ISFTIR and DFT results, it was found that  $\text{CO}_2$  is more favorable for the conversion to CO than  $\text{CH}_4$  due to the introduction of Cu single atoms. However, the photocatalytic activity of

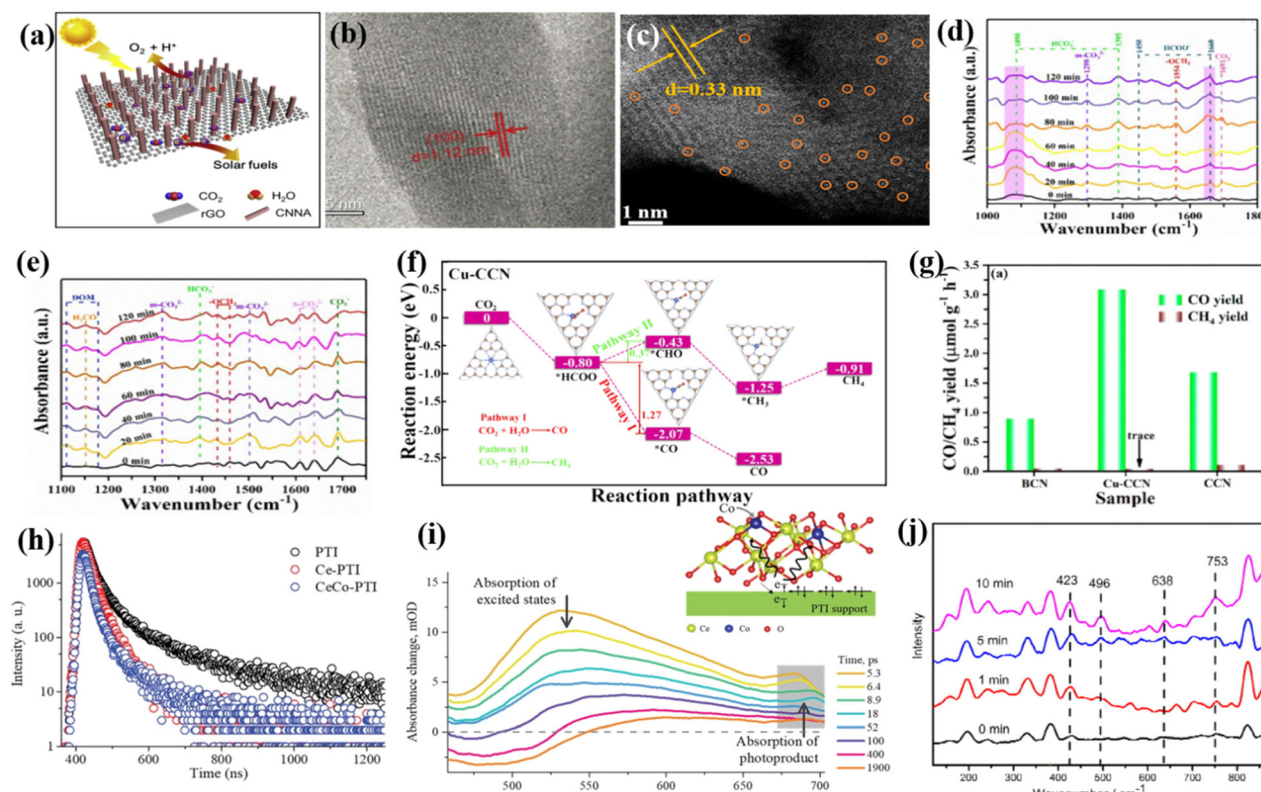


**Fig. 14** (a) 1D/2D CNNA/rGO. Reproduced from ref. 157 with permission from Elsevier, Copyright 2019. (b) HRTEM image of the inner structure of a CN nanorod in CNNA/r-GO. Reproduced from ref. 157 with permission from Elsevier, Copyright 2019. (c) HAADF-STEM image of Cu-CCN samples. Reproduced from ref. 158 with permission from the American Chemical Society, Copyright 2020. *In situ* Fourier transform infrared spectra (ISFTIR) of (d) Cu-CCN samples and (e) CCN samples. (f) Reaction pathways for photocatalytic  $\text{CO}_2$  reduction and the corresponding chemical molecular structure on Cu-CCN sample. Reproduced from ref. 158 with permission from the American Chemical Society, Copyright 2020. (g) Photocatalytic activity of samples for  $\text{CO}_2$  reduction. Reproduced from ref. 158 with permission from the American Chemical Society, Copyright 2020. (h) Time-resolved transient PL decay of PTI, Ce-PTI, and CeCo-PTI. (i) Femtosecond TA spectra of CeCo-PTI at different probe delays under 350 nm excitation. The inset shows interfacial electronic modification in CeCo-PTI. Reproduced from ref. 150 with permission from John Wiley-VCH, Copyright 2022. (j) *In situ* Raman spectra of CoTPP/g-C<sub>3</sub>N<sub>4</sub> in  $\text{CO}_2$ -saturated aqueous solution. Reproduced from ref. 168 with permission from The Royal Society of Chemistry, Copyright 2017.

highly crystalline g-C<sub>3</sub>N<sub>4</sub> is more likely to be enhanced after the introduction of single atoms due to the elimination of its defects. Thus, the Cu-CCN samples can achieve nearly 100% photocatalytic conversion of  $\text{CO}_2$  to CO (Fig. 14g).<sup>158</sup> Therefore, high-crystalline g-C<sub>3</sub>N<sub>4</sub>-based photocatalysts exhibit excellent effects and prospects in  $\text{CO}_2$  conversion. Differently, Cheng and her team proposed a new method to improve the photocatalytic  $\text{CO}_2$  reduction performance of highly crystalline g-C<sub>3</sub>N<sub>4</sub>. They constructed sigmoid heterojunctions with specific carrier migration by using single-atom Co anchored in a CeO<sub>2</sub> cocatalyst instead of a carbon nitride support. The specific unsaturated structure of bimetallic CeCo accelerated the movement of electrons from the PTI donor to the specific active site Co to achieve the directed electron transfer in specific interface structures, thus enabling the efficient photocatalytic conversion of  $\text{CO}_2$  to  $\text{CH}_4$ . Fig. 14(h and i) show the time-resolved transient PL decay and femtosecond transient absorption (fs-TA) spectra of CeCo-PTI, reflecting the decay kinetics of the dynamic charge separation in CeCo-PTI, which reduces the

charge recombination ability, and thus improves the catalytic performance.<sup>150</sup> Liu *et al.* designed and synthesized a compound of g-C<sub>3</sub>N<sub>4</sub> and cobalt porphyrin (CoTPP/g-C<sub>3</sub>N<sub>4</sub>) based on  $\pi$ - $\pi$  supramolecular interaction, and studied the formation of chemical bonds during  $\text{CO}_2$  reduction by *in situ* Raman testing in saturated  $\text{CO}_2$  solution (Fig. 14j). It was confirmed that the peaks at  $423\text{ cm}^{-1}$  and  $496\text{ cm}^{-1}$  were due to the insertion of active  $\text{CO}_2$  in the Co-C bond, and the peaks at  $638\text{ cm}^{-1}$  and  $753\text{ cm}^{-1}$  were due to the production of  $-\text{COO}^-$  and  $-\text{COOH}$  intermediates, respectively. The results showed that  $\text{CO}_2$  could be reduced to formic acid by the catalyst.<sup>168</sup>

## 5.2 Crystalline COFs for photocatalytic $\text{CO}_2$ reduction

Crystalline COF materials are promising porous crystal materials for artificial photosynthesis due to their tunable structures and chemical stability. Their large specific surface area provides more sites for  $\text{CO}_2$  adsorption and activation, and their ordered structure can effectively promote the efficient separation and transport of charge carriers.<sup>169</sup> For

instance, Lu *et al.* designed a series of crystalline porphyrinetrithiafulvalene covalent organic frameworks (TTCOF-M), in which the electron-deficient metalloporphyrin complexes (TAPP) possessed good visible light absorption ability and potential  $\text{CO}_2$  reduction ability, while the electron-rich tetra-thiafulvalene (TTF) possessed rapid electron transfer ability. The effective coupling between TAPP and TTF in the COFs

enables photogenerated electrons to be effectively separated and transferred from TTF to TAPP, thereby achieving redox center separation. TTCOF-Zn or TTCOF-Cu has a good photocatalytic redox potential for  $\text{CO}_2$  reduction because its conduction band minimum (CBM) is more negative than that of the standard reduction potential of  $\text{CO}/\text{CO}_2$ . The fast Fourier transformation image of the HRTEM image of TTCOF-Zn (Fig. 15a)

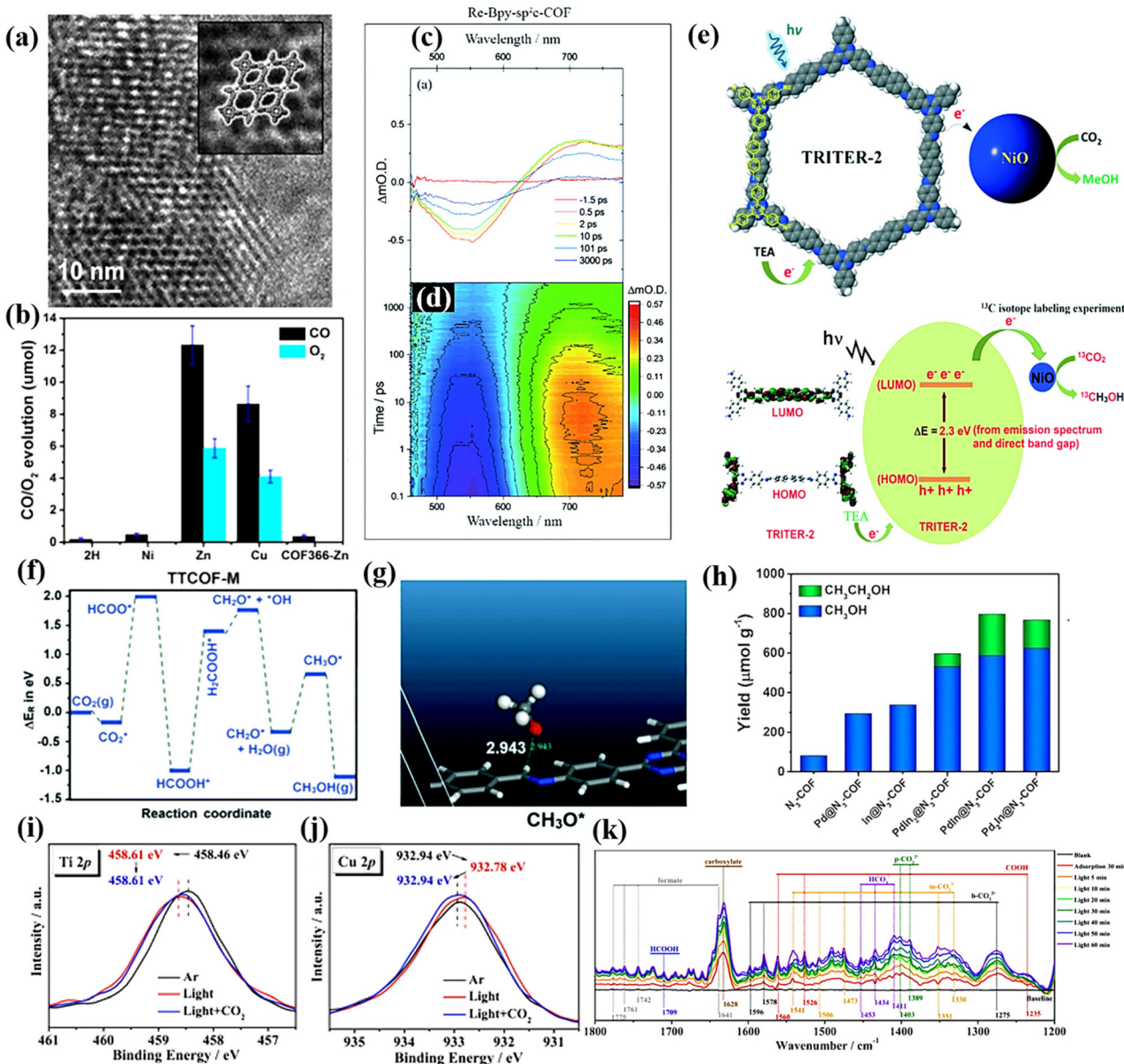


**Fig. 15** (a) HRTEM image of TTCOF-Zn, inset: the pores are highlighted. Reproduced from ref. 159 with permission from Wiley-VCH, Copyright 2019. (b)  $\text{CO}_2\text{RR}$  performances of TTCOF-M and COF366-Zn. Reproduced from ref. 159 with permission from Wiley-VCH, Copyright 2019. (c) Transient absorption spectra of Re-Bpy-sp<sup>2</sup>c-COF. Reproduced from ref. 160 with permission from The Royal Society of Chemistry, Copyright 2020. (d) Complete transient absorption surface probed Re-Bpy-sp<sup>2</sup>c-COF. Reproduced from ref. 160 with permission from The Royal Society of Chemistry, Copyright 2020. (e) Photocatalytic formation of methanol from  $\text{CO}_2$ . Reproduced from ref. 162 with permission from Elsevier, Copyright 2022. (f and g) Reaction energy for photocatalytic reduction of  $\text{CO}_2$ . Reproduced from ref. 162 with permission from Elsevier, Copyright 2022. (h) Photocatalytic performance for  $\text{CO}_2$  reduction of  $\text{Pd}_x\text{In}_y\text{N}_3\text{-COF}$ . Reproduced from ref. 71 with permission from Elsevier, Copyright 2021. (i and j) *In situ* XPS spectra of c Ti 2p and d Cu 2p for the simulated solar-driven  $\text{CO}_2$  reduction process over MCOF-Ti<sub>6</sub>Cu<sub>3</sub>. Reproduced from ref. 163 with permission from Springer Nature, Copyright 2022. (k) *In situ* DRIFTS spectra for the simulated solar-driven  $\text{CO}_2$  reduction process over MCOF-Ti<sub>6</sub>Cu<sub>3</sub>. Reproduced from ref. 163 with permission from Springer Nature, Copyright 2022.

showed its hexagonal void structure arranged along the axis of the 001 crystal, demonstrating its AA stacking pattern. This mode facilitated the transport of photogenerated electrons and holes and inhibited their recombination. The results showed that TTCOF-Zn exhibited excellent  $\text{CO}_2$  reduction capability in the absence of a photosensitizer, sacrificial agent and cocatalyst. Furthermore, TTCOF-Zn could achieve nearly 100%  $\text{CO}_2$  photoreduction to CO with only  $\text{H}_2\text{O}$  as the electron donor, with a maximum yield of  $12.33\ \mu\text{mol}$  after 60 h illumination (Fig. 15b).<sup>159</sup> Due to the covalent coupling between the TAPP and TTF molecules in TTCOFs, visible light induced the effective separation and transfer of  $e^-$ - $h^+$  pairs, which promoted the photocatalytic reaction. Moreover, due to the affinity between the metal and  $\text{CO}_2$  molecules, TTCOF-Zn had strong adsorption capacity for  $\text{CO}_2$ .

However, in many cases, additional sacrificial agents, photosensitizers, and cocatalysts are required to enhance the photocatalytic  $\text{CO}_2$  conversion ability of crystalline COFs. Fu *et al.* synthesized a bipyridine-containing crystalline  $\text{sp}^2\text{c}$ -COF, which was modified by a rhenium complex to improve its photocatalytic  $\text{CO}_2$  reduction performance. In this process, dye-sensitization played a critical role, enhancing the  $\text{CO}_2$  conversion capacity by 84% with a CO productivity of  $1040\ \mu\text{mol g}^{-1}\ \text{h}^{-1}$  over 17.5 h illumination. The transient absorption spectra (TA) (Fig. 15c and d) combined with the lifetime increase in the ground state bleach showed the formation of a long-lived charge separation state in Re- $\text{sp}^2\text{c}$ -COF. This also proved the high photocatalytic activity of the catalyst. Compared with the highly crystalline Re- $\text{sp}^2\text{c}$ -COF, the  $\text{CO}_2$  reduction activity of the analogous amorphous material was significantly reduced, which further confirmed the huge advantage of highly crystallized materials.<sup>160</sup> Yu *et al.* used the twisted binding of hexabenzocoronene (HBC) to form a dioxin-linked super stable two-dimensional high-crystalline COF (denoted as HBC-TFPN) with a wavy lattice. Increasing the crystallinity of covalent organic frame photocatalysts is beneficial to improve their photocatalytic activity. The results showed that in the presence of a photosensitizer and electron donor, the CO yield reached  $7.7\ \mu\text{mol g}^{-1}\ \text{h}^{-1}$  and the selectivity was as high as 92%.<sup>161</sup> Chakrabortty and colleagues synthesized recyclable crystalline ordered COFs based on triazine (TAPT) *via* the combined copolymerization of 4,4'-biphenyldicarbaldehyde and a triamine 1,3,5-tris-(4-aminophenyl) triazine. This highly crystalline organic polymer with excellent specific surface area and active sites could efficiently convert  $\text{CO}_2$  to methanol under the action of triethylamine electron donor and NiO cocatalyst (Fig. 15e). According to the energy calculation in the  $\text{CO}_2$  reduction process (Fig. 15f and g), the stable intermediate  $\text{HCOO}^*$  is formed by the hydrogenation of  $\text{CO}_2$ . The highest reaction energy of formic acid hydrogenation is the rate-determining step, and then the dissociated intermediate ( $\text{H}_2\text{COOH}^*$ ) is converted into hydroxyl ( $^*\text{OH}$ ) and formaldehyde (formaldehyde). Then, by further intermediate addition ( $\text{H}^*$ ), this process occurs until methanol is produced.<sup>162</sup> In the study of Huang *et al.*, they prepared highly crystalline COFs ( $\text{Pd}_x\text{In}_y@\text{N}_z$ -COF), which limited the growth

of PdIn nanoclusters. The highly conjugated structure of the highly crystalline COFs promotes carrier separation and the bi-metallic synergism stabilizes the  $\text{C}_1$  intermediate, which is more conducive to the formation of  $\text{C}_{2+}$  products. Therefore, the final products of photocatalytic  $\text{CO}_2$  conversion were mainly multi-carbon alcohols (Fig. 15h).<sup>71</sup> Zhou *et al.* prepared a crystalline skeleton material of heterometallic REDOX clusters based on a covalent organic framework, MCOF-Ti6Cu<sub>3</sub>, which effectively coupled photocatalytic  $\text{CO}_2$  reduction and water oxidation. The electron transfer process during the photocatalytic reaction was confirmed by *in situ* XPS test. As shown in Fig. 15i and j, upon exposure to illumination, the binding energy of Ti 2p increases, while that of Cu 2p decreases. More importantly, the binding energy changes to its initial value after  $\text{CO}_2$  is introduced, indicating that some of the electrons flow to the Cu cluster under photoexcitation and can undergo  $\text{CO}_2$  reduction reaction on the Cu cluster. *In situ* diffuse reflectance infrared Fourier transform spectroscopy (DRIFTS) (Fig. 15k) further elucidated the reason for its good photocatalytic performance and formic acid conversion selectivity. With an increase in the light exposure time, the  $^*\text{HCOOH}$  peak gradually increased, which is an important intermediate in the formation of HCOOH. This photocatalyst could convert  $\text{CO}_2$  to HCOOH with high selectivity.<sup>163</sup>

### 5.3 Crystalline CTFs for photocatalytic $\text{CO}_2$ reduction

Nitrogen-rich crystalline CTFs are promising photocatalytic  $\text{CO}_2$  conversion catalysts due to their high specific surface area, adjustable pore size and designable surface active sites. For instance, Huang *et al.* reported the preparation of a new catalyst *via* the photo-deposition of Pt on the surface of ethylene glycol (EG)-modified CTFs (PT-SA/CTF-1) (Fig. 16a). WT-EXAFS (Fig. 16b) further revealed the local coordination environment of the Pt-SA/CTF-1 catalyst, and the Pt-N structure provided the active site for photocatalytic  $\text{CO}_2$  reduction. CTF-1 is a crystalline material with a large specific surface area, which provides a scaffold for  $\text{CO}_2$  capture and activation. The modification of Pt single atoms not only improved the adsorption and activation of  $\text{CO}_2$ , but also accelerated the separation and transfer of photogenerated carriers in CTF-1, which enabled efficient photocatalytic  $\text{CO}_2$  methanation. Consequently, the yield of methane, as the main product, was about  $4.5\ \mu\text{mol g}^{-1}\ \text{h}^{-1}$  (Fig. 16c).<sup>164</sup> Moreover, He *et al.* reported a metal-free 2D/2D CN/CTF heterojunction with a long-range polymer framework for the highly selective conversion of  $\text{CO}_2$  to CO, reaching  $151.1\ \mu\text{mol g}^{-1}\ \text{h}^{-1}$  with a 30 h stabilization time (Fig. 16d). The enhanced photocatalytic activity is mainly attributed to the interaction of the two catalysts to generate a large number of photogenerated electrons, which also reduces the probability of charge recombination.<sup>145</sup>

### 5.4 Other crystalline organic polymeric materials for photocatalytic $\text{CO}_2$ reduction

In addition to the above-mentioned high-crystalline g-C<sub>3</sub>N<sub>4</sub>, COFs and CIFs, other high-crystalline organic polymeric materials have been reported for the photocatalytic conversion

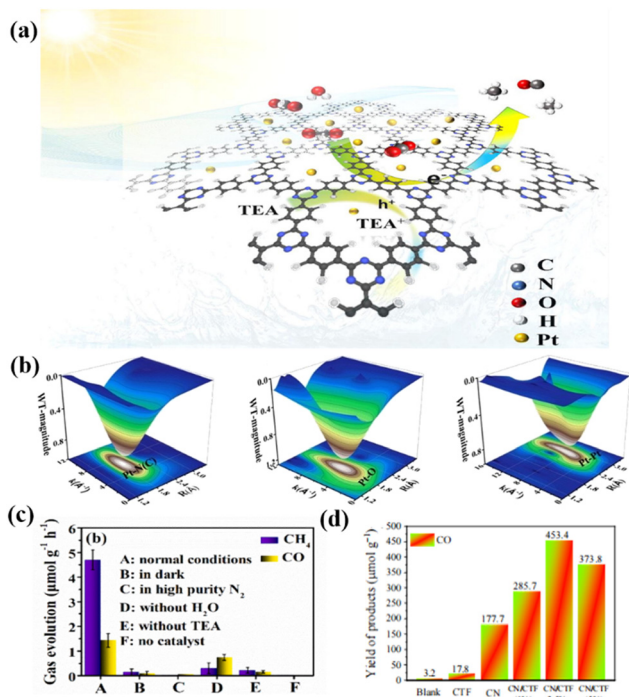


**Fig. 16** (a) Schematic illustration of the photocatalytic CO<sub>2</sub> reduction over Pt-SA/CTF-1 under visible light. Reproduced from ref. 164 with permission from Elsevier, Copyright 2021. (b) 3D contour WTEXAFS plots of Pt L<sub>3</sub>-edge EXAFS signals in Pt-SA/CTF-1 sample, PtO<sub>2</sub> and Pt foil. Reproduced from ref. 164 with permission from Elsevier, Copyright 2021. (c) CO<sub>2</sub> reduction performance under various conditions of Pt-SA/CTF-1. Reproduced from ref. 164 with permission from Elsevier, Copyright 2021. (d) Comparison of CO yield for CO<sub>2</sub> reduction under 200 mW cm<sup>-2</sup> visible light within 3 h with blank, CTF, CN, CN/CTF in acetonitrile/Co(bpy)<sub>3</sub>Cl<sub>2</sub> TEOA system. Reproduced from ref. 145 with permission from the Chinese Academy of Sciences, Copyright 2022.

of CO<sub>2</sub>. Verma *et al.* synthesized crystalline polymeric gels for photocatalytic CO<sub>2</sub> reduction *via* amide bond binding of tetra-thiafulvalene (TTF) and terpyridine (TPY) derivatives.<sup>170</sup> The ordered crystal structure led to an increase in  $\pi$ - $\pi$  stacking between the TTF and TPY molecules, which enhanced the visible light absorption range and promoted the photocatalytic CO<sub>2</sub> reduction.

## 6. Conclusions and outlook

Photocatalytic CO<sub>2</sub> conversion is increasingly becoming an effective way to convert waste carbon into high value-added clean energy and fuels, as well as a valid way to achieve carbon neutrality. In this process, compared with traditional inorganic semiconductor materials, high-crystalline conjugated organic polymeric materials (*e.g.*, g-C<sub>3</sub>N<sub>4</sub>, COFs, and CTFs) exhibit various advantages of tunable molecular or electronic structure, adjustable band gap by controlling different monomers, excellent visible light response, and unique properties of photocarrier separation and transport enabled by their  $\pi$ -conjugated stacking structures. Recently, an increasing

number of high-crystalline organic polymeric materials are being reported for photocatalytic reactions, such as water splitting for H<sub>2</sub>-evolution and CO<sub>2</sub> reduction. Compared with H<sub>2</sub>-evolution, photocatalytic CO<sub>2</sub> conversion is still in its infancy, and thus relatively less reported, but is attracting interest from a large number of researchers. In this review, we summarized the recent advances of high-crystalline conjugated organic polymeric materials in the conversion of CO<sub>2</sub> into high value-added chemical fuels *via* photocatalytic technology. Especially, the advantages of high-crystalline conjugated organic polymeric materials including absence of defects, enhanced built-in electric field, reduced interlayer hydrogen bonding, and crystal plane regulation were highlighted. The methods for the synthesis of crystalline g-C<sub>3</sub>N<sub>4</sub>, COFs, and CTFs were elaborated, such as molten-salt method, solid salt template method, microwave-assisted method, superacid-catalyzed strategy, and *in situ* oxidation. Subsequently, a series of methods for the modification of these materials was summarized to enhance their photocatalytic activities, which can give readers some reference and guidance. Finally, the applications of high-crystalline materials in photocatalytic CO<sub>2</sub> conversion were presented in detail.

Although some progress has been made in the preparation and application of highly crystalline conjugated organic polymeric materials, the related development in this field is still in its infancy, and the reported photocatalytic efficiencies are far from practical requirements. Some challenges and problems are faced in this research direction, which also shows great potential and prospects in many aspects:

(1) The current research is still focused on improving the yields of CO<sub>2</sub> conversion products, while there is a lack of in-depth research on product selectivity, conversion efficiency (such as turnover number (TON) and turnover frequency (TOF)), and solar energy utilization. In the case of the diversity of products (*e.g.*, CO, CH<sub>4</sub>, CH<sub>3</sub>OH, HCOOH, HCHO, C<sub>2</sub>H<sub>5</sub>OH, and C<sub>2</sub>H<sub>4</sub>), the rational design of photocatalysts is critical to improve their selectivity. Furthermore, the photoenzyme synergistic catalysis reaction that mimics plant photosynthesis is also a new approach for high-selectivity CO<sub>2</sub> conversion, in which the specificity and high activity of the enzyme can be combined.

(2) At present, the products of photocatalytic CO<sub>2</sub> conversion are still mainly C<sub>1</sub> derivatives, the most common ones are CO, CH<sub>4</sub> and HCOOH, mainly because these reaction processes are easier to realize. However, there are very few reports on higher value-added C<sub>2</sub> (*e.g.*, C<sub>2</sub>H<sub>5</sub>OH, C<sub>2</sub>H<sub>4</sub>, and C<sub>2</sub>H<sub>6</sub>) and multi-carbon (*e.g.*, polycarbon alcohols and polycarbon hydrocarbons) products, which have been achieved by methods such as electrocatalysis and thermocatalysis. More excitedly, some carbon and nitrogen compounds (such as urea and amino acids), which are the basic substances of life metabolism, are also expected to be realized through complex processes such as CO<sub>2</sub> conversion, C-C bond coupling, and C-N bond coupling. Therefore, various valuable carbon-containing products will be expected to be achieved by photocatalytic CO<sub>2</sub> conversion.

(3) To realize the practical application of the photocatalytic conversion of  $\text{CO}_2$  to high-value products and overcome the limitation of sunlight by alternating night-and-day, the combination of photocatalytic technology with solar photovoltaic, electrocatalysis and other technologies may be a meaningful way. Moreover, in this process, it is also very important for practical application to get rid of the dependence on cocatalysts, sacrificial agents, photosensitizers and organic solvents.

(4) Compared with crystalline  $\text{g-C}_3\text{N}_4$ , the species of crystalline COFs and CTFs are very few, and thus there is an urgent need to develop and prepare efficient crystalline COF and CTF photocatalysts for  $\text{CO}_2$  reduction, especially organic catalysts with spatially separated redox centers. In addition, the stability of high-crystalline conjugated organic polymeric materials need to be further improved.

(5) To deeply explore the molecular structure of high-crystalline conjugated organic polymeric catalysts and real-time tracking of their surface species changes during the photocatalytic  $\text{CO}_2$  conversion process to reveal the reaction mechanism, many advanced electronic and spectroscopic tools (e.g., synchrotron radiation-based XAFS spectroscopy, aberration-corrected scanning transmission electron microscopy, femtosecond transient absorption spectrometry (fs-TAS), and time-resolved fluorescence spectroscopy), *in situ* characterization techniques (e.g., *in situ* Raman, FTIR, and XPS) and DFT theoretical calculation are necessary.

In conclusion, high-crystalline conjugated organic polymeric materials have been proven to be excellent catalysts for photocatalytic  $\text{CO}_2$  conversion. Highly crystalline organic polymers will also be attractive for practical applications, which can provide some guidance to alleviate the environmental and energy issues. Combined with the in-depth understanding of the structure, properties and modification methods of high-crystalline organic polymers through more theoretical and experimental studies, more efficient high-crystalline organic polymers will be developed for photocatalytic  $\text{CO}_2$  reduction in the future.

## Author contributions

F. Y. wrote the draft of the manuscript, organized the figures, and selected the appropriate references. J. Q. and Y. Z. conceived the outline of the study. Y. C., X. Y. and C. M. Li revised the manuscript. J. H. conceived the theme and the outline of this manuscript, directed the research program, and revised the manuscript.

## Conflicts of interest

There are no conflicts to declare.

## Acknowledgements

We gratefully acknowledge the financial support provided by National Natural Science Foundation of China (22008163),

Postgraduate Research & Practice Innovation Program of Jiangsu Province, Natural Science Research Project of Higher Education Institutions in Jiangsu Province (20KJB150042 and 21KJB150038), Natural Science Foundation of Jiangsu Province (BK20210867), Doctor Project of Mass Entrepreneurship and Innovation in Jiangsu Province.

## References

- 1 M. Pera-Titus, *Chem. Rev.*, 2014, **114**, 1413–1492.
- 2 I. Sullivan, A. Goryachev, I. A. Digdaya, X. Li, H. A. Atwater, D. A. Vermaas and C. Xiang, *Nat. Catal.*, 2021, **4**, 952–958.
- 3 S. Sgouridis, M. Carbajales-Dale, D. Csala, M. Chiesa and U. Bardi, *Nat. Energy*, 2019, **4**, 456–465.
- 4 H. Zhou, Y. Zhang, W. Chen, W. Zhang and X. Lu, *Asian J. Org. Chem.*, 2022, **11**, 202100270.
- 5 P. Li, J. Bi, J. Liu, Q. Zhu, C. Chen, X. Sun, J. Zhang and B. Han, *Nat. Commun.*, 2022, **13**, 1–9.
- 6 K. M. Lee, J. H. Jang, M. Balamurugan, J. E. Kim, Y. I. Jo and K. T. Nam, *Nat. Energy*, 2021, **6**, 733–741.
- 7 E. Nikoloudakis, I. Lopez-Duarte, G. Charalambidis, K. Ladomenou, M. Ince and A. G. Coutsolelos, *Chem. Soc. Rev.*, 2022, **51**, 6965–7045.
- 8 J. Li, H. Huang, W. Xue, K. Sun, X. Song, C. Wu, L. Nie, Y. Li, C. Liu, Y. Pan, H. Jiang, D. Mei and C. Zhong, *Nat. Catal.*, 2021, **4**, 719–729.
- 9 J. Hou, G. Dong, B. Xiao, C. Malassigne and V. Chen, *J. Mater. Chem. A*, 2015, **3**, 3332–3342.
- 10 Z. Li, Y. Qu, J. Wang, H. Liu, M. Li, S. Miao and C. Li, *Joule*, 2019, **3**, 570–583.
- 11 P. Zhang, J. Hu, Y. Shen, X. Yang, J. Qu, F. Du, W. Sun and C. Li, *ACS Appl. Mater. Interfaces*, 2021, **13**, 46650–46658.
- 12 A. Fujishima and K. Honda, *Nature*, 1972, **238**, 37–38.
- 13 J. Hu, C. Chen, Y. Zheng, G. Zhang, C. Guo and C. Li, *Small*, 2020, **16**, 2002988.
- 14 Y. Shao, J. Hu, T. Yang, X. Yang, J. Qu, Q. Xu and C. Li, *Carbon*, 2022, **190**, 337–347.
- 15 C. Chen, J. Hu, X. Yang, T. Yang, J. Qu, C. Guo and C. Li, *ACS Appl. Mater. Interfaces*, 2021, **13**, 20162–20173.
- 16 H. Zhang, Y. Li, J. Wang, N. Wu, H. Sheng, C. Chen and J. Zhao, *Appl. Catal., B*, 2021, **284**, 119692.
- 17 Y. Feng, C. Wang, P. Cui, C. Li, B. Zhang, L. Gan, S. Zhang, X. Zhang, X. Zhou, Z. Sun, K. Wang, Y. Duan, H. Li, K. Zhou, H. Huang, A. Li, C. Zhuang, L. Wang, Z. Zhang and X. Han, *Adv. Mater.*, 2022, **34**, 2109074.
- 18 Y. Pan, Y. You, S. Xin, Y. Li, G. Fu, Z. Cui, Y. Men, F. Cao, S. Yu and J. B. Goodenough, *J. Am. Chem. Soc.*, 2017, **139**, 4123–4129.
- 19 S. Yin, X. Zhao, E. Jiang, Y. Yan, P. Zhou and P. Huo, *Energy Environ. Sci.*, 2022, **15**, 1556–1562.
- 20 A. Sabbah, I. Shown, M. Qorbani, F. Fu, T. Lin, H. Wu, P. Chung, C. Wu, S. R. M. Santiago, J. Shen, K. Chen and L. Chen, *Nano Energy*, 2022, **93**, 106809.

21 Y. Cao, R. Zhang, T. Zhou, S. Jin, J. Huang, L. Ye, Z. Huang, F. Wang and Y. Zhou, *ACS Appl. Mater. Interfaces*, 2020, **12**, 9935–9943.

22 R. Shankar, M. Sachs, L. Francàs, D. Lubert-Perquel, G. Kerhervé, A. Regoutz and C. Petit, *J. Mater. Chem. A*, 2019, **7**, 23931–23940.

23 X. Shi, X. A. Dong, Y. He, P. Yan and F. Dong, *Sci. Bull.*, 2022, **67**, 1137–1144.

24 X. Chen and A. Selloni, *Chem. Rev.*, 2014, **114**, 9281–9282.

25 Y. Ma, X. Wang, Y. Jia, X. Chen, H. Han and C. Li, *Chem. Rev.*, 2014, **114**, 9987–10043.

26 M. Sachs, R. S. Sprick, D. Pearce, S. A. J. Hillman, A. Monti, A. A. Y. Guilbert, N. J. Brownbill, S. Dimitrov, X. Shi, F. Blanc, M. A. Zwijnenburg, J. Nelson, J. R. Durrant and A. I. Cooper, *Nat. Commun.*, 2018, **9**, 4968.

27 D. Zhao, Y. Wang, C.-L. Dong, Y.-C. Huang, J. Chen, F. Xue, S. Shen and L. Guo, *Nat. Energy*, 2021, **6**, 388–397.

28 J. Hu, P. Zhang, T. Yang, Y. Cai, J. Qu and X. Yang, *Appl. Surf. Sci.*, 2022, **576**, 151841.

29 W. Zhang, L. Chen, S. Dai, C. Zhao, C. Ma, L. Wei, M. Zhu, S. Chong, H. Yang, L. Liu, Y. Bai, M. Yu, Y. Xu, X. Zhu, Q. Zhu, S. An, R. S. Sprick, M. A. Little, X. Wu, S. Jiang, Y. Wu, Y. Zhang, H. Tian, W. Zhu and A. I. Cooper, *Nature*, 2022, **604**, 72–79.

30 C. Wu, Z. Teng, C. Yang, F. Chen, H. B. Yang, L. Wang, H. Xu, B. Liu, G. Zheng and Q. Han, *Adv. Mater.*, 2022, **34**, 2110266.

31 K. Zhang, D. Kopetzki, P. H. Seeberger, M. Antonietti and F. Vilela, *Angew. Chem., Int. Ed.*, 2013, **52**, 1432–1436.

32 R. S. Sprick, J.-X. Jiang, B. Bonillo, S. Ren, T. Ratvijitvech, P. Guiglion, M. A. Zwijnenburg, D. J. Adams and A. I. Cooper, *J. Am. Chem. Soc.*, 2015, **137**, 3265–3270.

33 L. Li, Z. Cai, Q. Wu, W.-Y. Lo, N. Zhang, L. X. Chen and L. Yu, *J. Am. Chem. Soc.*, 2016, **138**, 7681–7686.

34 R. S. Sprick, B. Bonillo, R. Clowes, P. Guiglion, N. J. Brownbill, B. J. Slater, F. Blanc, M. A. Zwijnenburg, D. J. Adams and A. I. Cooper, *Angew. Chem., Int. Ed.*, 2016, **55**, 1792–1796.

35 F. He, Z. Wang, Y. Li, S. Peng and B. Liu, *Appl. Catal., B*, 2020, **269**, 118828.

36 Z. Xie, B. Wang, Z. Yang, X. Yang, X. Yu, G. Xing, Y. Zhang and L. Chen, *Angew. Chem., Int. Ed.*, 2019, **58**, 15742–15746.

37 P. Puthiaraj, Y.-R. Lee, S. Zhang and W.-S. Ahn, *J. Mater. Chem. A*, 2016, **4**, 16288–16311.

38 Z. Wang, Y. Luo, T. Hisatomi, J. J. M. Vequizo, S. Suzuki, S. Chen, M. Nakabayashi, L. Lin, Z. Pan, N. Kariya, A. Yamakata, N. Shibata, T. Takata, K. Teshima and K. Domen, *Nat. Commun.*, 2021, **12**, 1005.

39 L. Lin, Z. Lin, J. Zhang, X. Cai, W. Lin, Z. Yu and X. Wang, *Nat. Catal.*, 2020, **3**, 649–655.

40 H. Zhang, X. Chen, Z. Zhang, K. Yu, W. Zhu and Y. Zhu, *Appl. Catal., B*, 2021, **287**, 119957.

41 W. Iqbal, B. Qiu, Q. Zhu, M. Xing and J. Zhang, *Appl. Catal., B*, 2018, **232**, 306–313.

42 X. Lin, H. Du, D. Jiang, P. Zhang, Z. Yu, H. Bi and Y. Yuan, *J. Energy Chem.*, 2022, **65**, 541–547.

43 J. Xiao, X. Liu, L. Pan, C. Shi, X. Zhang and J.-J. Zou, *ACS Catal.*, 2020, **10**, 12256–12283.

44 M. Mansha, T. Ahmad, N. Ullah, S. A. Khan, M. Ashraf, S. Ali, B. Tan and I. Khan, *Chem. Rec.*, 2022, **22**, e202100336.

45 X. Wang, K. Maeda, A. Thomas, K. Takanabe, G. Xin, J. M. Carlsson, K. Domen and M. Antonietti, *Nat. Mater.*, 2009, **8**, 76–80.

46 E. Wirnhier, M. Doblinger, D. Gunzelmann, J. Senker, B. V. Lotsch and W. Schnick, *Chemistry*, 2011, **17**, 3213–3221.

47 L. Lin, H. Ou, Y. Zhang and X. Wang, *ACS Catal.*, 2016, **6**, 3921–3931.

48 Y. Xu, X. He, H. Zhong, D. J. Singh, L. Zhang and R. Wang, *Appl. Catal., B*, 2019, **246**, 349–355.

49 M. J. Bojdys, J.-O. Muller, M. Antonietti and A. Thomas, *Chem. – Eur. J.*, 2008, **14**, 8177–8182.

50 F. K. Kessler, Y. Zheng, D. Schwarz, C. Merschjann, W. Schnick, X. Wang and M. J. Bojdys, *Nat. Rev. Mater.*, 2017, **2**, 17030.

51 M. Liu, C. Wei, H. Zhuzhang, J. Zhou, Z. Pan, W. Lin, Z. Yu, G. Zhang and X. Wang, *Angew. Chem., Int. Ed.*, 2022, **61**, 202113389.

52 Y. Li, D. Zhang, X. Feng and Q. Xiang, *Chin. J. Catal.*, 2020, **41**, 21–30.

53 M. K. Bhunia, K. Yamauchi and K. Takanabe, *Angew. Chem., Int. Ed.*, 2014, **53**, 11001–11005.

54 E. Kroke, M. Schwarz, E. Horath-Bordon, P. Kroll, B. Noll and A. D. Norman, *New J. Chem.*, 2002, **26**, 508–512.

55 J. Gracia and P. Kroll, *J. Mater. Chem.*, 2009, **19**, 3013.

56 D. Dontsova, S. Pronkin, M. Wehle, Z. Chen, C. Fettkenhauer, G. Clavel and M. Antonietti, *Chem. Mater.*, 2015, **27**, 5170–5179.

57 J. Hu, C. Chen, H. Yang, F. Yang, J. Qu, X. Yang, W. Sun, L. Dai and C. Li, *Appl. Catal., B*, 2022, **317**, 121723.

58 C. Qiu, Y. Xu, X. Fan, D. Xu, R. Tandiana, X. Ling, Y. Jiang, C. Liu, L. Yu, W. Chen and C. Su, *Adv. Sci.*, 2019, **6**, 1801403.

59 J. Yuan, Y. Tang, X. Yi, C. Liu, C. Li, Y. Zeng and S. Luo, *Appl. Catal., B*, 2019, **251**, 206–212.

60 G. Zhang, J. Zhu, Y. Xu, C. Yang, C. He, P. Zhang, Y. Li, X. Ren and H. Mi, *ACS Catal.*, 2022, **12**, 4648–4658.

61 T. Huo, Q. Deng, F. Yu, G. Wang, Y. Xia, H. Li and W. Hou, *ACS Appl. Mater. Interfaces*, 2022, **14**, 13419–13430.

62 F. Guo, B. Hu, C. Yang, J. Zhang, Y. Hou and X. Wang, *Adv. Mater.*, 2021, **33**, 2101466.

63 T. Yang, Y. Shao, J. Hu, J. Qu, X. Yang, F. Yang and C. Li, *Chem. Eng. J.*, 2022, **448**, 137613.

64 Y. Yuan, L. Yin, S. Cao, L. Gu, G. Xu, P. Du, H. Chai, Y. Liao and C. Xue, *Green Chem.*, 2014, **16**, 4663–4668.

65 L. Lin, P. Ye, C. Cao, Q. Jin, G. Xu, Y. Shen and Y. Yuan, *J. Mater. Chem. A*, 2015, **3**, 10205–10208.

66 Q. Liu, X. Wang, Q. Yang, Z. Zhang and X. Fang, *Appl. Catal., B*, 2018, **225**, 22–29.

67 X. Li, J. Zhang, X. Chen, A. Fischer, A. Thomas, M. Antonietti and X. Wang, *Chem. Mater.*, 2011, **23**, 4344–4348.

68 A. P. Cote, A. I. Benin, N. W. Ockwig, M. O’Keeffe, A. J. Matzger and O. M. Yaghi, *Science*, 2005, **310**, 1166–1170.

69 Q. Yang, M. Luo, K. Liu, H. Cao and H. Yan, *Appl. Catal., B*, 2020, **276**, 119174.

70 F. J. Uribe-Romo, C. J. Doonan, H. Furukawa, K. Oisaki and O. M. Yaghi, *J. Am. Chem. Soc.*, 2011, **133**, 11478–11481.

71 Y. Huang, P. Du, W.-X. Shi, Y. Wang, S. Yao, Z.-M. Zhang, T.-B. Lu and X. Lu, *Appl. Catal., B*, 2021, **288**, 120001.

72 S. Kandambeth, D. B. Shinde, M. K. Panda, B. Lukose, T. Heine and R. Banerjee, *Angew. Chem., Int. Ed.*, 2013, **52**, 13052–13056.

73 X. Chen, M. Addicoat, E. Jin, L. Zhai, H. Xu, N. Huang, Z. Guo, L. Liu, S. Irle and D. Jiang, *J. Am. Chem. Soc.*, 2015, **137**, 3241–3247.

74 X. Li, J. Qiao, S. Chee, H. Xu, X. Zhao, H. S. Choi, W. Yu, S. K. Quek, U. Mirsaidov and K. P. Loh, *J. Am. Chem. Soc.*, 2020, **142**, 4932–4943.

75 C. O. Kappe, *Angew. Chem., Int. Ed.*, 2004, **43**, 6250–6284.

76 N. L. Campbell, R. Clowes, L. K. Ritchie and A. I. Cooper, *Chem. Mater.*, 2009, **21**, 204–206.

77 H. Wei, S. Chai, N. Hu, Z. Yang, L. Wei and L. Wang, *Chem. Commun.*, 2015, **51**, 12178–12181.

78 R. Matsuoka, R. Sakamoto, K. Hoshiko, S. Sasaki, H. Masunaga, K. Nagashio and H. Nishihara, *J. Am. Chem. Soc.*, 2017, **139**, 3145–3152.

79 K. Dey, M. Pal, K. C. Rout, H. S. Kunjattu, A. Das, R. Mukherjee, U. K. Kharul and R. Banerjee, *J. Am. Chem. Soc.*, 2017, **139**, 13083–13091.

80 D. D. Medina, J. M. Rotter, Y. Hu, M. Dogru, V. Werner, F. Auras, J. T. Markiewicz, P. Knochel and T. Bein, *J. Am. Chem. Soc.*, 2015, **137**, 1016–1019.

81 B. P. Biswal, S. Chandra, S. Kandambeth, B. Lukose, T. Heine and R. Banerjee, *J. Am. Chem. Soc.*, 2013, **135**, 5328–5331.

82 G. Li, J. Ye, Q. Fang and F. Liu, *Chem. Eng. J.*, 2019, **370**, 822–830.

83 W. Zhao, P. Yan, H. Yang, M. Bahri, A. M. James, H. Chen, L. Liu, B. Li, Z. Pang, R. Clowes, N. D. Browning, J. W. Ward, Y. Wu and A. I. Cooper, *Nat. Synth.*, 2022, **1**, 87–95.

84 P. Kuhn, M. Antonietti and A. Thomas, *Angew. Chem., Int. Ed.*, 2008, **47**, 3450–3453.

85 M. J. Bojdys, J. Jeromenok, A. Thomas and M. Antonietti, *Adv. Mater.*, 2010, **22**, 2202–2205.

86 Z.-A. Lan, M. Wu, Z. Fang, Y. Zhang, X. Chen, G. Zhang and X. Wang, *Angew. Chem., Int. Ed.*, 2022, **61**, 202201482.

87 Z. Yang, H. Chen, S. Wang, W. Guo, T. Wang, X. Suo, D. E. Jiang, X. Zhu, I. Popovs and S. Dai, *J. Am. Chem. Soc.*, 2020, **142**, 6856–6860.

88 J. Liu, P. Lyu, Y. Zhang, P. Nachtigall and Y. Xu, *Adv. Mater.*, 2018, **30**, 1705401.

89 K. Wang, L. Yang, X. Wang, L. Guo, G. Cheng, C. Zhang, S. Jin, B. Tan and A. Cooper, *Angew. Chem., Int. Ed.*, 2017, **56**, 14149–14153.

90 V. Nguyen and M. Grunwald, *J. Am. Chem. Soc.*, 2018, **140**, 3306–3311.

91 J. Liu, M. Liu, X. Wang, X. Wang and B. Tan, *Small*, 2022, **18**, 2200984.

92 M. Liu, Q. Huang, S. Wang, Z. Li, B. Li, S. Jin and B. Tan, *Angew. Chem., Int. Ed.*, 2018, **57**, 11968–11972.

93 S.-Y. Yu, J. C. Kim, H.-J. Noh, Y.-K. Im, J. Mahmood, I.-Y. Jeon, S. K. Kwak and J.-B. Baek, *Cell Rep. Phys. Sci.*, 2021, **2**, 100653.

94 S.-Y. Yu, J. Mahmood, H.-J. Noh, J.-M. Seo, S.-M. Jung, S.-H. Shin, Y.-K. Im, I. I.-Y. Jeon and J.-B. Baek, *Angew. Chem., Int. Ed.*, 2018, **57**, 8438–8442.

95 S. Chu, Y. Wang, C. Wang, J. Yang and Z. Zou, *Int. J. Hydrogen Energy*, 2013, **38**, 10768–10772.

96 J. Liu, W. Zan, K. Li, Y. Yang, F. Bu and Y. Xu, *J. Am. Chem. Soc.*, 2017, **139**, 11666–11669.

97 M. S. Lohse and T. Bein, *Adv. Funct. Mater.*, 2018, **28**, 1705553.

98 J. Wang, Z. Yang, W. Yao, X. Gao and D. Tao, *Appl. Catal., B*, 2018, **238**, 629–637.

99 X. Bu, Y. Bu, S. Yang, F. Sun, L. Tian, Z. Peng, P. He, J. Sun, T. Huang, X. Wang, G. Ding, J. Yang and X. Xie, *RSC Adv.*, 2016, **6**, 112210–112214.

100 S. Y. Ding and W. Wang, *Chem. Soc. Rev.*, 2013, **42**, 548–568.

101 U. Diebold, *Nat. Chem.*, 2011, **3**, 271–272.

102 J. Ge, J. Zheng, J. Zhang, S. Jiang, L. Zhang, H. Wan, L. Wang, W. Ma, Z. Zhou and R. Ma, *J. Mater. Chem. A*, 2021, **9**, 14432–14443.

103 F. Jiang, S. Wang, B. Liu, J. Liu, L. Wang, Y. Xiao, Y. Xu and X. Liu, *ACS Catal.*, 2020, **10**, 11493–11509.

104 M. Dimitrievska, F. Oliva, M. Guc, S. Giraldo, E. Saucedo, A. Pérez-Rodríguez and V. Izquierdo-Roca, *J. Mater. Chem. A*, 2019, **7**, 13293–13304.

105 D. Edelberg, D. Rhodes, A. Kerelsky, B. Kim, J. Wang, A. Zangiabadi, C. Kim, A. Abhinandan, J. Ardelean, S. Scully, D. Scullion, L. Embon, R. Zu, E. J. G. Santos, L. Balicas, C. Marianetti, K. Barmak, X. Zhu, J. Hone and A. N. Pasupathy, *Nano Lett.*, 2019, **19**, 4371–4379.

106 Y. Liu, C. Chen, Y. He, Z. Zhang, M. Li, C. Li, X.-B. Chen and Z. Shi, *Small*, 2022, 2201556, DOI: [10.1002/smll.202201556](https://doi.org/10.1002/smll.202201556).

107 M. Denecke, *Coord. Chem. Rev.*, 2006, **250**, 730–754.

108 C. S. Fadley, *J. Electron Spectrosc. Relat. Phenom.*, 2010, **178–179**, 2–32.

109 M. Kalbac, Y. P. Hsieh, H. Farhat, L. Kavan, M. Hofmann, J. Kong and M. S. Dresselhaus, *Nano Lett.*, 2010, **10**, 4619–4626.

110 D. A. Muller, *Nat. Mater.*, 2009, **8**, 263–270.

111 F. Tuomisto and I. Makkonen, *Rev. Mod. Phys.*, 2013, **85**, 1583–1631.

112 G. Gabrielse, D. Hanneke, T. Kinoshita, M. Nio and B. Odom, *Phys. Rev. Lett.*, 2006, **97**, 030802.

113 N. A. Khan, R. Zhang, X. Wang, L. Cao, C. S. Azad, C. Fan, J. Yuan, M. Long, H. Wu, M. A. Olson and Z. Jiang, *Nat. Commun.*, 2022, **13**, 1–8.

114 J. Li, L. Cai, J. Shang, Y. Yu and L. Zhang, *Adv. Mater.*, 2016, **28**, 4059–4064.

115 Y. Guo, W. Shi and Y. Zhu, *EcoMat*, 2019, **1**, 12007.

116 Z. Zhang, X. Chen, H. Zhang, W. Liu, W. Zhu and Y. Zhu, *Adv. Mater.*, 2020, **32**, 1907746.

117 J. Li, G. Zhan, Y. Yu and L. Zhang, *Nat. Commun.*, 2016, **7**, 11480.

118 Y. Guo, S. Huang, Y. Guo, Z. Ye, J. Nan, Q. Zhou and Y. Zhu, *Appl. Catal., B*, 2022, **312**, 121388.

119 J. Wang, Y. Yu, J. Cui, X. Li, Y. Zhang, C. Wang, X. Yu and J. Ye, *Appl. Catal., B*, 2022, **301**, 120814.

120 W. Ren, J. Cheng, H. Ou, C. Huang, M. M. Titirici and X. Wang, *ChemSusChem*, 2019, **12**, 3257–3262.

121 Y. Wang, M. Sun, W. Tang, Q. Li, Z. Ren, Y. Liu, Y. Zhang, C. Zeng, Z. Wang, Y. Wu, J. Hao, X. Wu and R. Yang, *Mater. Today Phys.*, 2022, **23**, 100634.

122 B. Zhao, D. Gao, Y. Liu, J. Fan and H. Yu, *J. Colloid Interface Sci.*, 2022, **608**, 1268–1277.

123 X. Liu, B. Jing, G. Lun, Y. Wang, X. Wang, C. Fang, Z. Ao and C. Li, *Chem. Commun.*, 2020, **56**, 3179–3182.

124 S. Shen, J. Chen, Y. Wang, C. Dong, F. Meng, Q. Zhang, Y. Huangfu, Z. Lin, Y. Huang, Y. Li, M. Li and L. Gu, *Sci. Bull.*, 2022, **67**, 520–528.

125 L. Cheng, P. Zhang, Q. Wen, J. Fan and Q. Xiang, *Chin. J. Catal.*, 2022, **43**, 451–460.

126 S. Cao, H. Li, T. Tong, H.-C. Chen, A. Yu, J. Yu and H. Chen, *Adv. Funct. Mater.*, 2018, **28**, 1802169.

127 J. Zhang, C. Yu, J. Lang, Y. Zhou, B. Zhou, Y. Hu and M. Long, *Appl. Catal., B*, 2020, **277**, 119225.

128 S. Li, M. Wu, T. Guo, L. Zheng, D. Wang, Y. Mu, Q. Xing and J. Zou, *Appl. Catal., B*, 2020, **272**, 118989.

129 C. Zhu, Q. Fang, R. Liu, W. Dong, S. Song and Y. Shen, *Environ. Sci. Technol.*, 2022, **56**, 6699–6709.

130 Y. Chen, X. Yan, J. Xu and L. Wang, *J. Mater. Chem. A*, 2021, **9**, 24056–24063.

131 Z. Luo, C. Li, S. Liu, T. Wang and J. Gong, *Chem. Sci.*, 2017, **8**, 91–100.

132 G. Zhang, Y. Xu, D. Yan, C. He, Y. Li, X. Ren, P. Zhang and H. Mi, *ACS Catal.*, 2021, **11**, 6995–7005.

133 S. Wu, H. Yu, S. Chen and X. Quan, *ACS Catal.*, 2020, **10**, 14380–14389.

134 J. Li, P. Liu, Y. Tang, H. Huang, H. Cui, D. Mei and C. Zhong, *ACS Catal.*, 2020, **10**, 2431–2442.

135 G. Huang, G. Lin, Q. Niu, J. Bi and L. Wu, *J. Mater. Sci. Technol.*, 2022, **116**, 41–49.

136 Z. Mi, T. Zhou, W. Weng, J. Unruangsri, K. Hu, W. Yang, C. Wang, K. A. I. Zhang and J. Guo, *Angew. Chem., Int. Ed.*, 2021, **60**, 9642–9649.

137 T. Zhou, L. Wang, X. Huang, J. Unruangsri, H. Zhang, R. Wang, Q. Song, Q. Yang, W. Li, C. Wang, K. Takahashi, H. Xu and J. Guo, *Nat. Commun.*, 2021, **12**, 3934.

138 L. Chen, L. Wang, Y. Wan, Y. Zhang, Z. Qi, X. Wu and H. Xu, *Adv. Mater.*, 2020, **32**, 1904433.

139 X. Li, J. Hu, T. Yang, X. Yang, J. Qu and L. C, *Nano Energy*, 2022, **92**, 106714.

140 R. Marschall, *Adv. Funct. Mater.*, 2014, **24**, 2421–2440.

141 L. Zhang, J. Zhang, H. Yu and J. Yu, *Adv. Mater.*, 2022, **34**, 2107668.

142 H. Li, Y. Zhou, W. Tu, J. Ye and Z. Zou, *Adv. Funct. Mater.*, 2015, **25**, 998–1013.

143 Q. Xu, L. Zhang, B. Cheng, J. Fan and J. Yu, *Chem.*, 2020, **6**, 1543–1559.

144 Y. Li, F. Gong, Q. Zhou, X. Feng, J. Fan and Q. Xiang, *Appl. Catal., B*, 2020, **268**, 118381.

145 J. He, C. Wang, X. Jin, S. Liu, Q. Zhao and M. Zhu, *Chin. J. Catal.*, 2022, **43**, 1306–1315.

146 Y. Lin, X. Wang, X. Fu and W. Su, *J. Mater. Chem. A*, 2022, **10**, 8252–8257.

147 Z. Zeng, H. Yu, X. Quan, S. Chen and S. Zhang, *Appl. Catal., B*, 2018, **227**, 153–160.

148 Z. Sun, H. Dong, Q. Yuan, Y. Tan, W. Wang, Y. Jiang, J. Wan, J. Wen, J. Yang, J. He, T. Cheng and L. Huang, *Chem. Eng. J.*, 2022, **435**, 134865.

149 N. Xu, Y. Liu, W. Yang, J. Tang, B. Cai, Q. Li, J. Sun, K. Wang, B. Xu, Q. Zhang and Y. Fan, *ACS Appl. Energy Mater.*, 2020, **3**, 11939–11946.

150 L. Cheng, X. Yue, J. Fan and Q. Xiang, *Adv. Mater.*, 2022, **34**, 2200929.

151 S. Mehla, A. E. Kandjani, R. Babarao, A. F. Lee, S. Periasamy, K. Wilson, S. Ramakrishna and S. K. Bhargava, *Energy Environ. Sci.*, 2021, **14**, 320–352.

152 Z. Zhang, G. Wen, D. Luo, B. Ren, Y. Zhu, R. Gao, H. Dou, G. Sun, M. Feng, Z. Bai, A. Yu and Z. Chen, *J. Am. Chem. Soc.*, 2021, **143**, 6855–6864.

153 V. D. Luca, D. Vullo, A. Scozzafava, V. Carginale, M. Rossi, C. T. Supuran and C. Capasso, *Bioorg. Med. Chem.*, 2013, **21**, 1465–1469.

154 Z. Wen, S. Xu, Y. Zhu, G. Liu, H. Gao, L. Sun and F. Li, *Angew. Chem., Int. Ed.*, 2022, **61**, e202201086.

155 Y. Wang, Y. Qu, B. Qu, L. Bai, Y. Liu, Z. Yang, W. Zhang, L. Jing and H. Fu, *Adv. Mater.*, 2021, **33**, 2105482.

156 G. Zhang, G. Li, T. Heil, S. Zafeiratos, F. Lai, A. Savateev, M. Antonietti and X. Wang, *Angew. Chem., Int. Ed.*, 2019, **58**, 3433–3437.

157 Y. Xia, Z. Tian, T. Heil, A. Meng, B. Cheng, S. Cao, J. Yu and M. Antonietti, *Joule*, 2019, **3**, 2792–2805.

158 Y. Li, B. Li, D. Zhang, L. Cheng and Q. Xiang, *ACS Nano*, 2020, **14**, 10552–10561.

159 M. Lu, J. Liu, Q. Li, M. Zhang, M. Liu, J. Wang, D. Yuan and Y. Lan, *Angew. Chem., Int. Ed.*, 2019, **58**, 12392–12397.

160 Z. Fu, X. Wang, A. M. Gardner, X. Wang, S. Y. Chong, G. Neri, A. J. Cowan, L. Liu, X. Li, A. Vogel, R. Clowes, M. Bilton, L. Chen, R. S. Sprick and A. I. Cooper, *Chem. Sci.*, 2020, **11**, 543–550.

161 H.-Y. Yu, J.-S. Wang, F.-Y. Xie, Q. Yang, Y. Chen, L. Zhao, Y. Li and W.-J. Ruan, *Chem. Eng. J.*, 2022, **445**, 136713.

162 P. Chakrabortty, S. Ghosh, A. Das, A. Khan and S. M. Islam, *Catal. Sci. Technol.*, 2022, **12**, 3484–3497.

163 J. Zhou, J. Li, L. Kan, L. Zhang, Q. Huang, Y. Yan, Y. Chen, J. Liu, S. L. Li and Y. Q. Lan, *Nat. Commun.*, 2022, **13**, 4681.

164 G. Huang, Q. Niu, J. Zhang, H. Huang, Q. Chen, J. Bi and L. Wu, *Chem. Eng. J.*, 2022, **427**, 131018.

165 J. Hu, T. Yang, X. Yang, J. Qu, Y. Cai and C. Li, *Small*, 2022, **18**, 2105376.

166 H. Li, B. Zhu, S. Cao and J. Yu, *Chem. Commun.*, 2020, **56**, 5641–5644.

167 P. Xia, M. Antonietti, B. Zhu, T. Heil, J. Yu and S. Cao, *Adv. Funct. Mater.*, 2019, **29**, 1900093.

168 J. Liu, H. Shi, Q. Shen, C. Guo and G. Zhao, *Green Chem.*, 2017, **19**, 5900–5910.

169 S. Yang, W. Hu, X. Zhang, P. He, B. Pattengale, C. Liu, M. Cendejas, I. Hermans, X. Zhang, J. Zhang and J. Huang, *J. Am. Chem. Soc.*, 2018, **140**, 14614–14618.

170 P. Verma, A. Singh, F. A. Rahimi, P. Sarkar, S. Nath, S. K. Pati and T. K. Maji, *Nat. Commun.*, 2021, **12**, 1–14.